Systematic differences in energy radiation processes between regular and inland low-frequency earthquakes in and around the focal area of the 2008 M_w 6.9 Iwate-Miyagi, Japan, earthquake

Masaki Orimo[1*], Keisuke Yoshida[1], Toru Matsuzawa[1], Taka'aki Taira[2], Kentaro Emoto[3], Akira Hasegawa[1]

[1] Research Center for Prediction of Earthquakes and Volcanic Eruptions, Graduate School of Science, Tohoku University, Sendai, Japan

[2] Berkeley Seismological Laboratory, University of California, Berkeley, California, U.S.A.

[3] Institute of Seismology and Volcanology, Kyushu University, Fukuoka, Japan

[*]Corresponding author: Masaki Orimo (masaki.orimo.s2@dc.tohoku.ac.jp)

Key Points:

- We conducted spectral analysis to quantify scaled energy for regular and low-frequency earthquakes (LFEs)
- The scaled energy of LFEs are one to three orders of magnitude lower than that of regular earthquakes.
- The local magnitudes for the LFEs show good agreement with the energy magnitudes, but large discrepancy with the seismic moment magnitudes.

Abstract

Many unknowns exist regarding the energy radiation processes of the inland low-frequency earthquakes (LFEs) often observed beneath volcanoes. To evaluate their energy radiation characteristics, we estimated the scaled energy for LFEs and regular earthquakes in and around the focal area of the 2008 M_w 6.9 Iwate-Miyagi earthquake. We computed the source spectra for regular earthquakes, deep LFEs, and shallow LFEs by correcting for the site and path effects from direct S-waves. We computed the radiated energy and seismic moment, and obtained the scaled energy (e_R) for 1464 regular earthquakes, 169 deep LFEs, and 52 shallow LFEs. The e_R for regular earthquakes is in the order of 10^{-5} to 10^{-4}, typical for crustal earthquakes, and tends to become smaller near volcanoes and shallow LFEs. In contrast, e_R is in the order of 10^{-7} and 10^{-6} for deep and shallow LFEs, respectively, one to three orders of magnitude smaller than that for regular earthquakes. This result suggests that LFEs are associated with a much lower stress drop and/or slower rupture and deformation rates than regular earthquakes. Although the energy magnitudes derived from radiated energy generally show good agreement with the local magnitudes for the three types of earthquakes, the moment and local magnitudes show a large discrepancy for the LFEs. This suggests that the local magnitude based only on the maximum amplitude of the observed seismic records may not provide good information on the static sizes of LFEs whose e_R values are substantially different from those of regular earthquakes.

Plain Language Summary

Low-frequency earthquakes (LFEs) beneath volcanoes have unique characteristics such as a much lower dominant frequency than regular earthquakes with similar magnitudes and long-lasting trailing parts. Although previous studies have suggested that magma or fluid may be related to the generation of LFEs, the details of seismic wave radiation processes are not as well understood for LFEs. One key parameter for evaluating the energy radiation characteristics is the scaled energy (e_R). Here, we estimated e_R for regular earthquakes and LFEs in and around the focal area of the 2008 M_w 6.9 Iwate-Miyagi earthquake. We found that the e_R values for regular earthquakes were in the order of 10^{-5}, which is consistent with previous studies. However, the e_R values for the LFEs were one to three orders of magnitude lower than those of regular earthquakes. These results suggest that LFEs are associated with smaller stress drops and/or slower rupture and deformation rates than are regular earthquakes. Furthermore, our results show that owing to this difference in e_R, the local magnitude, which is based on the maximum amplitude of the seismic waves, cannot adequately represent the static sizes of the LFEs.

1 Introduction

A special type of earthquake called a deep low-frequency earthquake (deep LFE) has markedly different characteristics from regular earthquakes. They have a very low dominant frequency compared with regular earthquakes of similar magnitude (e.g., Ukawa and Ohtake, 1987; Hasegawa and Yamamoto,1994; Obara, 2002; Katsumata and Kamaya, 2003; Rogers and Dragert, 2003). Some occur in the transition zone between the unstable and stable slip zones along the plate boundary (e.g., Obara 2002; Katsumata and Kamaya, 2003; Rogers and Dragert, 2003), while others occur around the Moho discontinuity in the continental plate, often beneath volcanoes (e.g., Ukawa and Ohatke, 1987; Hasegawa and Yamamoto, 1994). The first type of deep LFEs represent shear faulting along the plate boundary (e.g., Shelly et al., 2006, 2007; Ide et al. 2007b), whereas many unknowns exist regarding the seismic wave radiation processes of latter deep LFEs called inland deep LFEs. The Japan Meteorological Agency (JMA) routinely locates regular earthquakes and deep LFEs in and around the Japanese Islands and determines their local magnitudes (M_{jma}; M_{jma} indicates the JMA magnitude scale) using a nationwide seismic network (e.g., Kamaya and Katsumata 2004). This study focuses on inland deep LFEs.

Inland deep LFEs have a very low dominant frequency compared to regular earthquakes with similar magnitudes and characteristic long-lasting high-amplitude trailing parts (e.g., Hasegawa and Yamamoto, 1994). They often occur in or at the margins of low seismic wave velocity regions, which may reflect magma or fluid dehydration from magma (e.g., Hasegawa et al., 1991; Hasegawa and Yamamoto, 1994; Nakajima et al., 2001). Previous studies have suggested that deep LFEs may be related to magmatic or fluid activities such as magma movement (e.g., Aki and Koyanagi, 1981; Ukawa and Ohtake, 1987; Hasegawa and Yamamoto, 1994; Aso et al., 2013), fluid movement (e.g., Hasegawa et al., 2005; Wech et al., 2020), fluid-induced oscillations (e.g., Aki et al., 1977; Julian, 1994; Aso and Ide, 2014), cooling magma (e.g., Aso and Tsai, 2014) and failure along a tensile-shear crack (e.g., Nakamichi et al., 2003).

Most deep inland LFEs have been observed beneath volcanoes around the Moho discontinuity (e.g., Ukawa and Ohatke, 1987; Hasegawa and Yamamoto, 1994). However, some recent studies have reported that earthquakes with dominant frequencies much lower than those of regular earthquakes of similar magnitude also occur in the upper crust, very close to the locations of regular earthquakes (e.g., Baltay et al., 2011; Kosuga and Haruyama, 2018; Yoshida et al., 2020; Nakajima and Hasegawa, 2021; Tsuchiyama et al., 2022). Yoshida et al. (2020) showed that deep LFEs with long-lasting high-amplitude trailing parts in Hakodate, Hokkaido, Japan, are distributed continuously from the lower crust to the upper crust, and that the LFEs in the upper crust occur within a few kilometers of regular earthquakes. Nakajima and Hasegawa (2021) systematically analyzed small earthquakes with $0 \leq M_{jma} \leq 2.5$ in the upper crust in Japan. They found that several earthquakes, whose dominant frequencies were much lower than those of regular earthquakes of similar magnitudes, occurred very close to regular earthquakes. We refer to these earthquakes as "shallow low-frequency earthquakes (shallow LFEs)," according to Nakajima and Hasegawa (2021) and Hasegawa and Nakajima (2022). Previous studies have proposed that fluid movement stemming from the subducting slab (Yoshida et al., 2020) or crustal fluid redistribution due to recent large earthquakes (Nakajima and Hasegawa, 2021; Tsuchiyama et al., 2022) may be related to the generation of these shallow LFEs in the upper crust.

Previous studies have suggested that magma or crustal fluids may be responsible for the generation of inland deep and shallow LFEs (e.g., Ukawa and Ohtake, 1987; Hasegawa and Yamamoto, 1994; Hasegawa et al., 2005; Aso et al., 2013; Yoshida et al., 2020; Nakajima and Hasegawa, 2021; Tsuchiyama et al., 2022). However, the details of the seismic wave radiation processes of LFEs are still poorly understood compared with those of regular earthquakes, which are essentially fault ruptures. Although dominant frequencies of LFEs are much lower than those of regular earthquakes of similar magnitudes (e.g., Hasegawa and Yamamoto, 1994), few quantitative evaluations have been conducted on the source properties of LFEs. To understand the seismic wave radiation processes of LFEs, it is necessary to quantify their seismic radiation energy. Traditionally, stress drops based on earthquake corner frequencies have been used to characterize the source properties of small regular earthquakes (e.g., Shearer et al., 2006; Trugman and Shearer, 2017; Yoshida et al., 2017; Trugman, 2020; Shearer et al., 2022), assuming the ω^2-model (Aki, 1967; Brune, 1970). However, some previous studies have suggested that the radiation processes of LFEs may not be consistent with the ω^2 model (e.g., Ide et al., 2007a; Yoshida et al., 2020). Thus, we here use seismic radiated energy to characterize the radiation properties of LFEs because any assumptions on radiation pattern, such as a specific shape of source spectrum like the Brune-type ω^2 model (Brune, 1970) or a specific value of rupture speed, are not required to estimate radiated energy.

In and around the focal area of the 2008 M_w 6.9 Iwate-Miyagi earthquake, many deep LFEs (20–40 km) have been observed beneath volcanoes around the Moho discontinuity (e.g., Hasegawa and Yamamoto, 1994) (Figure 1 and Figure 2). This area is surrounded by many borehole seismic stations, and recent studies have identified relocated hypocenters for small earthquakes (e.g., Okada et al., 2012; Yoshida et al., 2014a) in this region, making it suitable for studying the source properties of earthquakes (Figure 1 and Figure 3). Nakajima and Hasegawa (2021) reported that shallow LFEs (~ 10 km) also occur in and around this area (Figure 1 and Figure 2). The nature of shallow LFEs is also not yet clear, but it is easier to study their source characteristics than to study deep LFEs because they occur in the upper crust and the path effects are similar to those of regular earthquakes. In this study, the scaled energy of regular earthquakes, deep LFEs, and shallow LFEs was estimated to investigate their radiation properties.

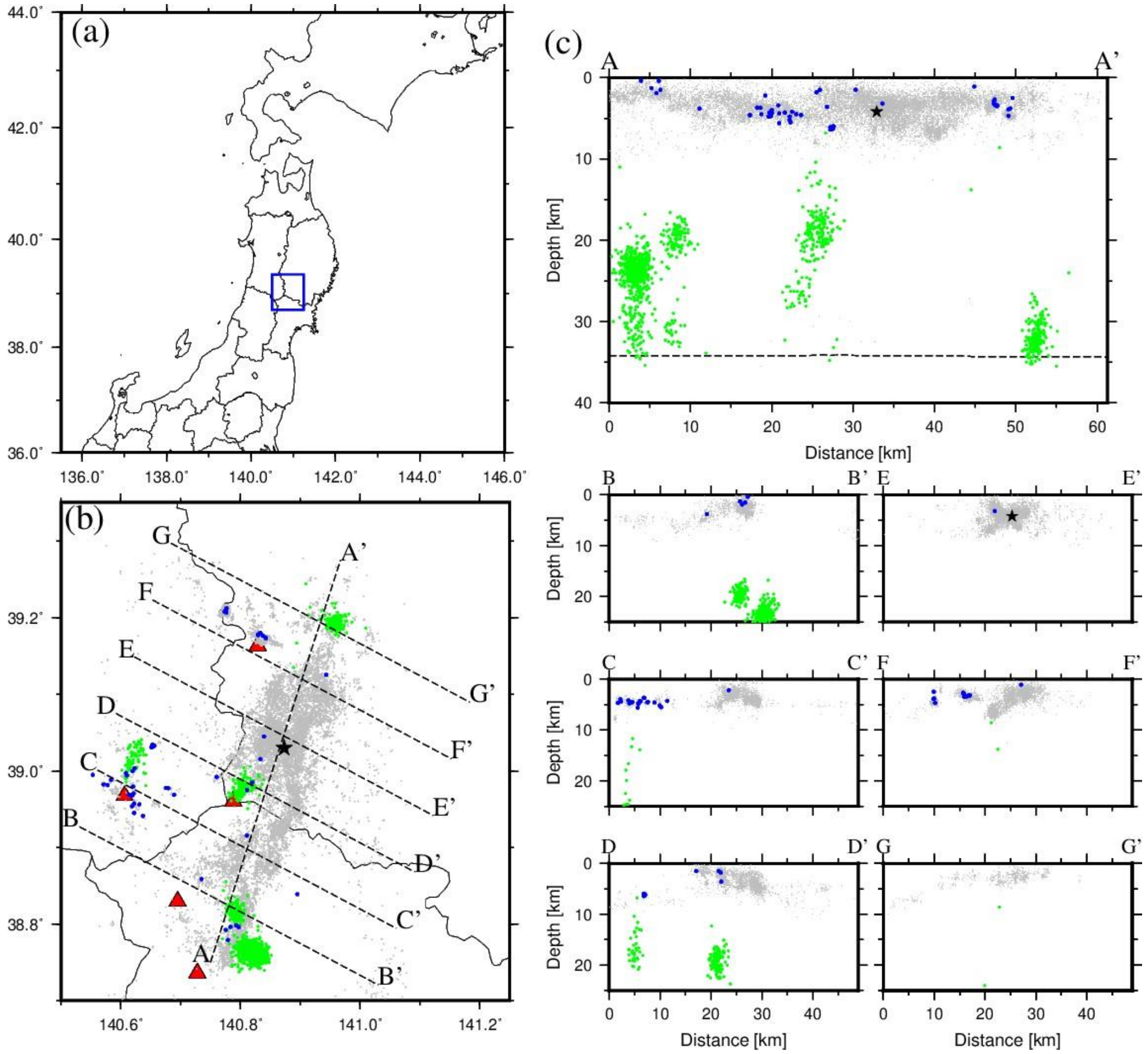

Figure 1. Hypocenter distribution in and around the focal area of the 2008 M_w 6.9 Iwate-Miyagi earthquake. (a) Map of NE Japan. (b) Epicentral distribution in the region shown by a blue rectangle in (a). (c) Vertical cross-section along the line A–A' to G–G'. Gray and blue circles indicate regular earthquakes ($M_{jma} \geq 1.0$) and shallow LFEs, respectively (Nakajima and Hasegawa, 2021) for the period from 1 March, 2003 to 31 December, 2010. Green circles indicate deep LFEs identified by JMA for the period from1 March, 2003 to31 December, 2020. A black star indicates the hypocenter of the 2008 M_w 6.9 Iwate-Miyagi earthquake. Red triangles indicate volcanoes. The black dashed line in line A–A' indicates the Moho discontinuity (Zhao et al., 1990). Note that we used the hypocenter data from the relocated catalog by Yoshida et al. (2014a) for the regular earthquakes and the shallow LFEs, and the JMA unified catalog for deep LFEs.

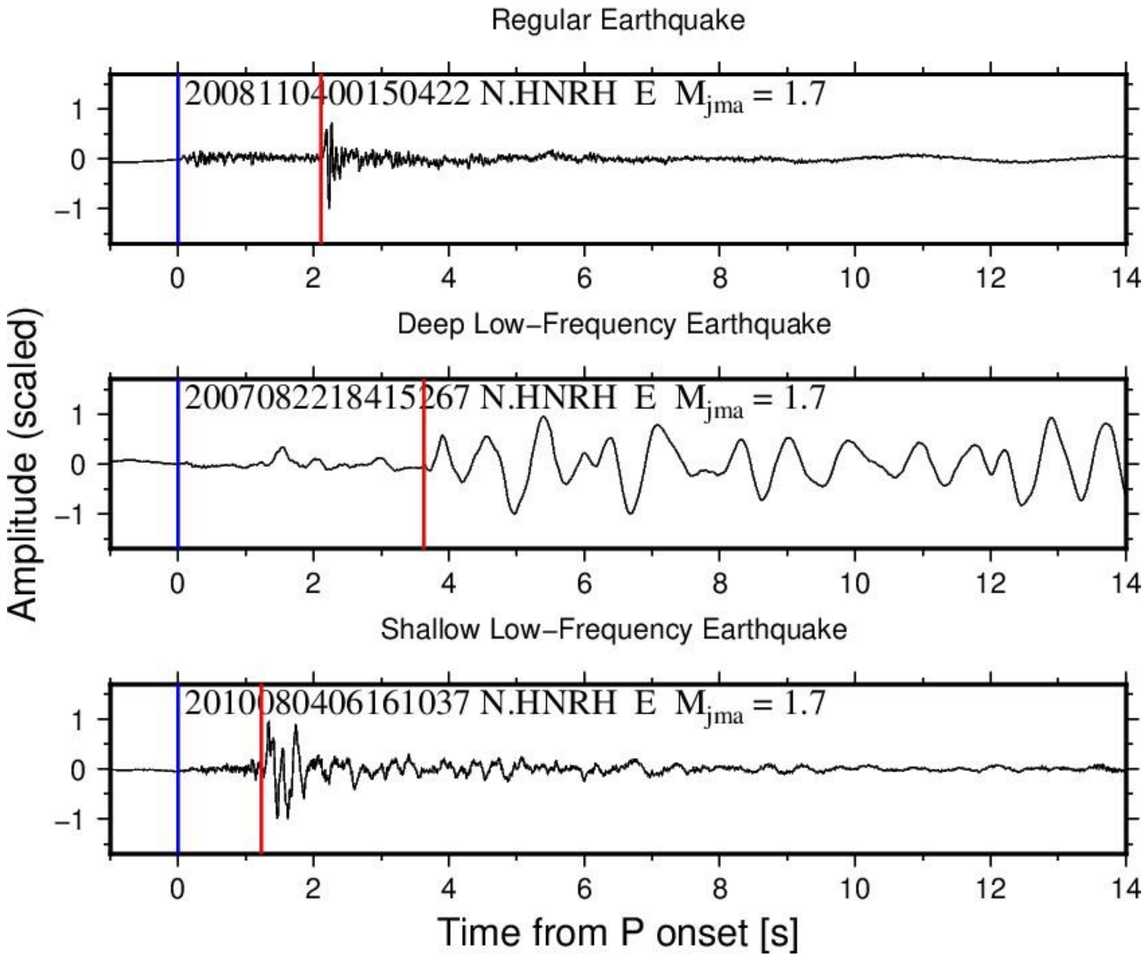

Figure 2. Examples of E-W-component waveforms of the regular earthquake, the deep LFE and the shallow LFE at N. HNRH. Waveforms are 0.2 Hz high-pass filtered and normalized by their respective maximum amplitudes. The blue and red lines indicate the onsets of the P- and S-waves respectively.

2 Data and Methods

2-1 Station and events

We analyzed S-wave spectra to obtain the scaled energy for 3560 regular earthquakes ($M_{jma} \geq 2.0$) and 52 shallow LFEs (Nakajima and Hasegawa, 2021) for the period from 1 March, 2003 to 31 December, 2010 and 1086 deep LFEs for the period from 1 March, 2003 to 31 December, 2020. We used hypocenter data from the relocated catalog by Yoshida et al. (2014a) for regular earthquakes and shallow LFEs, and the JMA unified catalog for deep LFEs. Note that we did not analyze regular earthquakes and shallow LFEs whose hypocenters were not relocated by Yoshida et al. (2014a), even though the earthquakes were listed in the JMA unified catalog.

We obtained three-component (E-W, N-S, and U-D) waveform data from the velocity-type seismometers surrounding the focal area of the 2008 Iwate-Miyagi earthquake (Figure 3). Their natural frequencies were 1 Hz (except for TU.KWT, whose natural frequency was 0.05 Hz), and the sampling frequency was 100 Hz. We corrected the instrumental characteristics of the seismometers to obtain velocity waveforms.

We used information from the JMA catalog for the onset times of P- and S-waves, set the time window length to 3.3 s from the time 0.3 s before S-wave onset, and computed the spectral amplitudes of the three components using FFT. We also calculated the noise spectral amplitudes for each station and component with the time window length at 3.3 s from the time 3.5 s before P-wave onset, and computed the signal-to-noise amplitude ratios (SNRs) for each station and component. We used the spectral amplitudes only if the SNRs at all frequency points from 0.5 Hz to 20 Hz were larger than 3.0 for the regular earthquakes, and 1.5 for the deep and shallow LFEs. We discarded events for which less than twelve and three spectra were available for regular earthquakes, deep LFEs, and shallow LFEs, respectively.

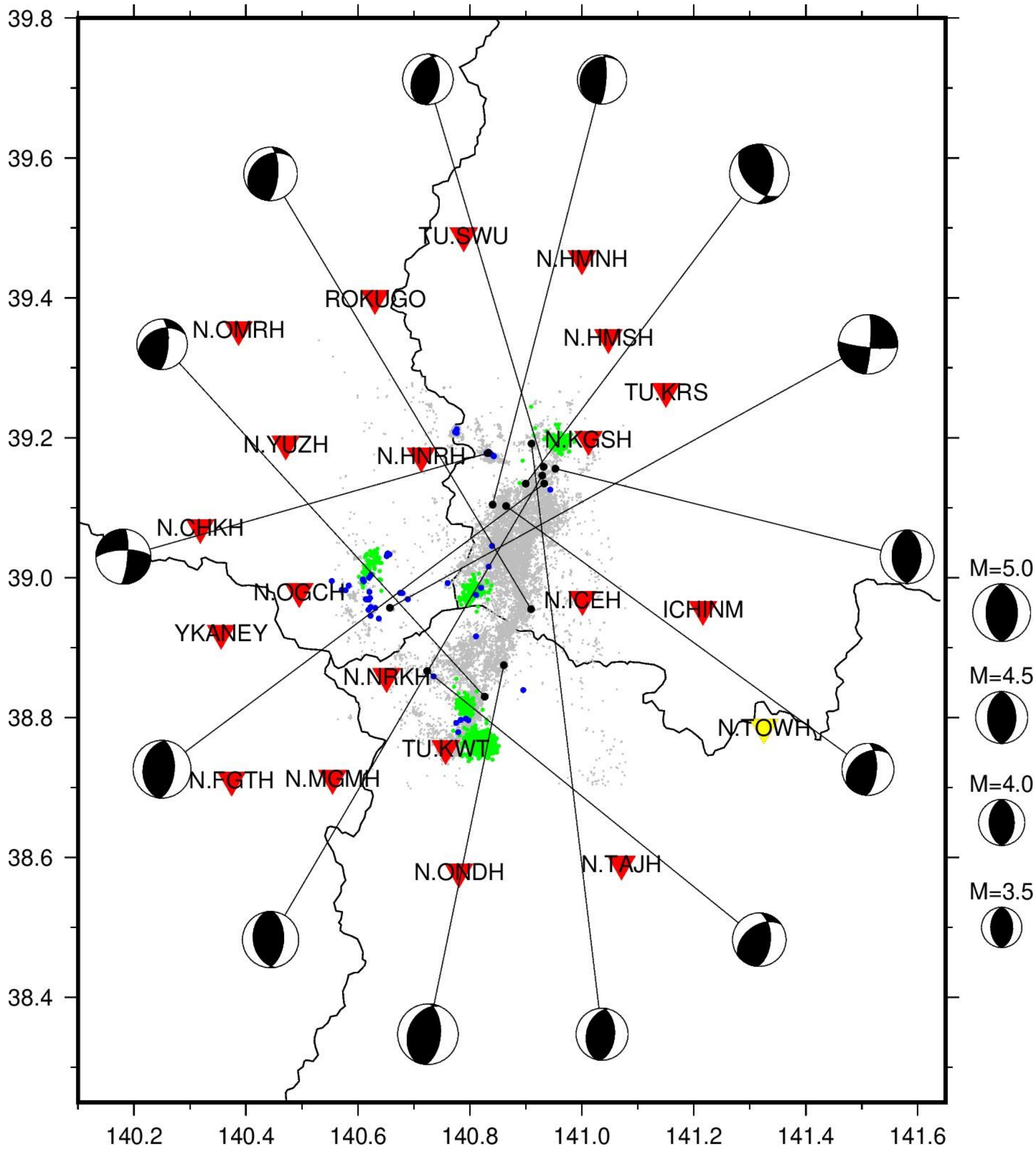

Figure 3. Distribution of the seismic stations. Red inverted triangles indicate the stations used in this study. Yellow inverted triangle (N. TOWH) indicates a station used in this study and a reference station for the coda normalization method in section 2-3. Gray and blue

circles indicate the regular earthquakes ($M_{jma} \geq 1.0$) and the shallow LFEs for the period from 1 March, 2003 to 31 December, 2010, respectively. Green circles indicate the deep LFEs identified by JMA for the period from 1 March, 2003 to 31 December, 2020. Black circles indicate the 14 regular earthquakes used to estimate the site response and attenuation factors. The beach balls indicate the focal mechanisms of the 14 events determined by the National Research Institute for Earth Science and Disaster Resilience (NIED) F-net moment tensor catalog. Note that we used the hypocenter data from the relocated catalog by Yoshida et al. (2014a) for the regular earthquakes and the shallow LFEs, and the JMA unified catalog for the deep LFEs

2-2 Source spectrum

We estimated the seismic-scale energy e_R for regular earthquakes, deep LFEs, and shallow LFEs using their source spectra to investigate the radiation properties of the LFEs. e_R is the ratio of the radiated energy E_R to the seismic moment M_0,

$$e_R = \frac{E_R}{M_0} \tag{1}$$

and has been used to investigate the seismic radiation process between earthquakes of different magnitudes (e.g., Kanamori et al., 1993; Abercrombie,1995; Prieto et al., 2004; Yoshida and Kanamori, 2023). In this study, we separately estimated E_R and M_0 using the source spectrum to obtain e_R.

We determined the source spectrum from the observed velocity spectra for each earthquake to calculate E_R and M_0. The observed velocity spectrum $v_i(f)$ at the ith station at frequency f can be expressed using its source spectrum $S(f)$

$$v_i(f) = \frac{2\pi f S(f) G_i(f) P_i(f) R_{\theta\varphi i} F_{si}}{4\pi\rho\beta^3 r_i} \tag{2}$$

where $G_i(f)$ is the site response factor for the ith seismic station, $P_i(f)$ is the attenuation term, $R_{\theta\phi i}$ is the radiation pattern of the S-wave, F_{si} is the reflection effect from the free surface, r_i is hypocentral distance, β is the S-wave velocity around the source and ρ is the mean crustal density at 2.7 $\mathrm{g/cm^3}$, respectively. $P_i(f)$ can be expressed using the frequency-dependent attenuation term along a ray path from the source to the station ($t^*(f)$):

$$P_i(f) = \exp\left(-\pi f t^*(f)\right) \tag{3}$$

where

$$t^*(f) = \int_{source}^{receiver} \frac{Q^{-1}(f,s)}{\beta(s)} ds \tag{4}$$

where $Q^{-1}(f,s)$ and $\beta(s)$ are the attenuation factor at frequency f and S-wave velocity along the ray path s, respectively. We used the 1-D S-wave velocity structure proposed by Ueno et al. (2002). We assumed $R_{\theta\phi i}$ as the root mean square (RMS) value of a point shear dislocation $R_{\theta\phi i} = R_{\theta\phi i}^{RMS} = \sqrt{2/5}$ and F_{si} as 2 for all frequency points at all stations.

The source spectrum was calculated by correcting for site and path effects from the observed velocity spectra (Takahashi et al., 2005; Yoshida et al., 2017). We determined the site response factor $G_i(f)$ and the attenuation factor Q^{-1} using the coda normalization method (Aki and Chouet, 1975; Aki, 1980). We describe the data and methods used to estimate the site response factors in sections 2-3 and 2-5-2, the data and method to estimate the attenuation factor in section 2-4 and the method for calculating the source spectrum, radiated energy, seismic moment, and scaled energy for each earthquake in section 2-5-3.

2-3 Site response factor

The site response factors for the three components were estimated based on the coda normalization method proposed by Aki and Chouet (1975). We assumed that the coda wave at a lapse time longer than twice the direct S-wave travel time did not depend on the radiation pattern or hypocentral distance because the seismic energy was spatially homogeneously distributed at that time (Aki and Chouet, 1975). The coda-wave spectral amplitude $A_i(f, t_c)$ at the ith station at frequency f at lapse time t_c ($t_c > 2t_{si}$, where t_{si} is the S-wave travel time at the ith station) can be written in terms of its source spectrum $S(f)$ and site response factor $G_i(f)$ as

$$A_i(f, t_c) = S(f)C(f, t_c)G_i(f) \tag{5}$$

where $C(f, t_c)$ is the coda excitation factor characterizing medium heterogeneity, which is only dependent on frequency and lapse time and is independent of the source station locations. Taking the ratio of the coda spectral amplitudes between different stations for the same event at a common lapse time (t_c) from the original time, the ratio is equivalent to the ratio of the site response factors between the two stations.

$$\frac{A_i(f, t_c)}{A_j(f, t_c)} = \frac{S(f)C(f, t_c)G_i(f)}{S(f)C(f, t_c)G_j(f)} = \frac{G_i(f)}{G_j(f)} \tag{6}$$

To estimate the site response factors for three components, we selected 14 regular earthquakes with $M_{jma} \geq 3.5$ whose rupture processes are simple, based on apparent source time functions determined by Yoshida and Kanamori (2023), and used their coda spectral amplitudes. We fixed t_c at 45 s for all stations, components, frequency points, and events, and set the time window length to be 5.12 s. We removed the waveform records contaminated by other earthquakes beforehand and used only the waveforms whose SNRs at all frequency points from 0.5 Hz to 20 Hz were larger than 3.0.

Because we could not obtain the absolute value of the site response factors based on this method, we set a reference station located at a hard-rock site. The site response factor for the reference station was assumed to be 1 for each frequency point and component. We selected the station installed in the rock with the highest S-wave velocity (Yoshida et al., 2017), according to the core log data of the NIED Hi-net as the reference station (N. TOWH). For each component, we estimated the relative site response factors for the other stations by taking the logarithm of equation (6) for all station pairs and applying the least-squares method. Verification of the site response factor at the reference station is described in section 2-5-2.

Figure 4 shows the site response factors obtained for each station and their components. Most stations in this study were borehole stations. Most stations on the hard rock site ($V_s > 1000\ \mathrm{m/s}$) showed a site response factor similar to that of the reference station. In contrast, stations located on soft sites ($V_s < 1000\ \mathrm{m/s}$) tended to have a larger site response factor at low frequencies ($f < 2\ \mathrm{Hz}$) which decreased with frequency at higher frequencies ($f > 2$ Hz).

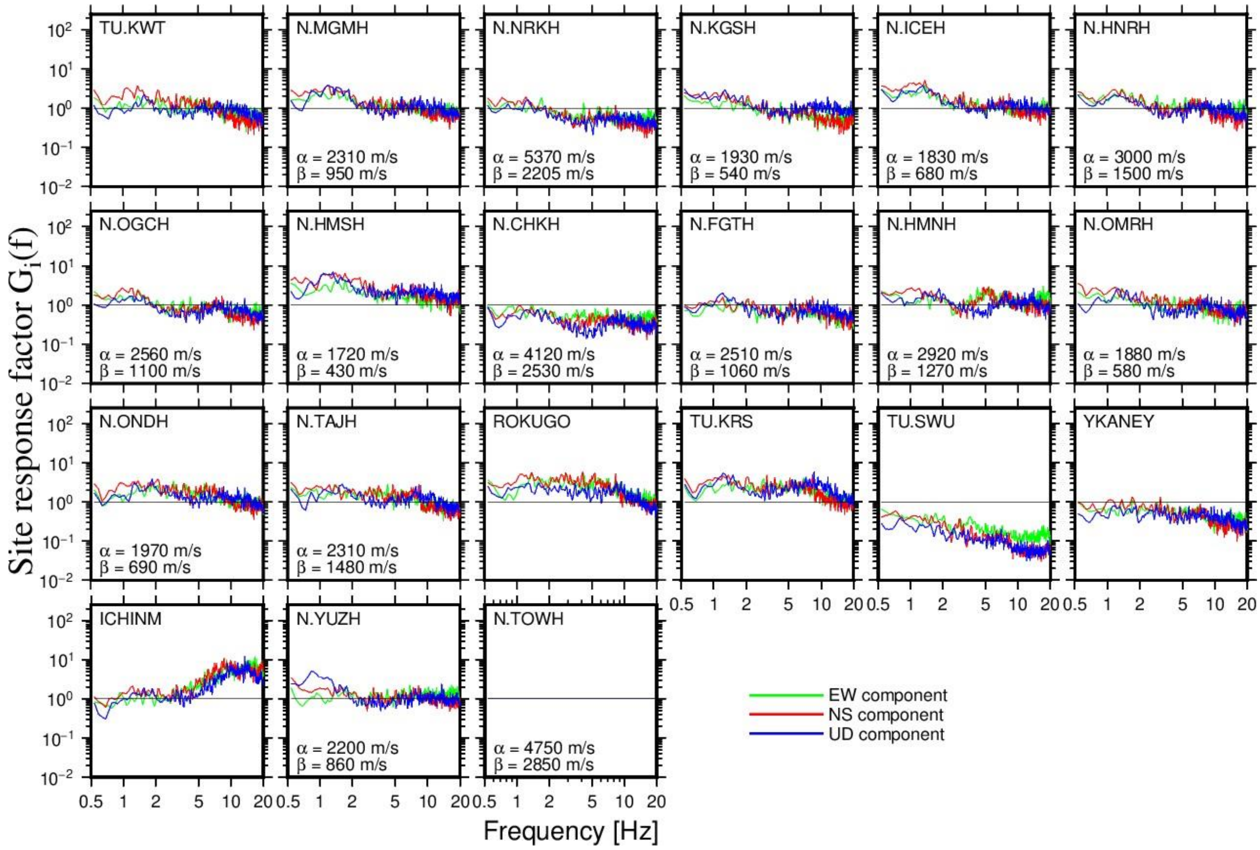

Figure 4. Estimated relative site response factors in comparison to that for the reference station. The green, red, and blue lines indicate the estimated relative site response factors for the east-west, north-south and vertical components respectively. α and β represent the P- and S-wave velocities at the stations listed on the Hi-net columnar maps, respectively.

2-4 Attenuation factor

We assumed a spatially homogeneous attenuation factor Q^{-1} in the entire region and estimated the attenuation factor Q^{-1} for each frequency point based on the coda normalization method proposed by Aki (1980). This method is based on the distance decay of the S-wave amplitude, other than on geometrical spreading. By normalizing the direct S-wave spectral amplitude by the coda wave spectral amplitude, we can cancel the site and source effects on the observed waveforms and isolate the attenuation factor Q^{-1} (Aki, 1980) as

$$\ln\left(\frac{v_i(f)r_i}{A_i(f,t_c)}\right) = -\pi f Q^{-1}(f)\, t_{si} + const \quad (7)$$

We determined $-\pi f Q^{-1}$ from the linear slope of the left side of equation (7) against the S-wave travel-time t_{si} (Figure 5-a) using least-square method and estimated Q^{-1}. We used three components of the S-wave and coda waveforms of the 14 earthquakes described in section 2-3 and calculated the left side of equation (7) for each station and component. We adopted the same method for selecting the spectra as described in sections 2-1 and 2-3. We estimated the Q^{-1}-value from 0.5 Hz to 20 Hz at 0.1 Hz intervals.

Figure 5 shows the estimated frequency-dependent attenuation factor Q^{-1} based on the coda normalization method. The estimated Q^{-1} decays with the frequency (Figure 5-b). We approximated the frequency-dependent attenuation factor using the Q-value at 1 Hz (Q_0^{-1}) and the frequency-dependence factor (a) by fitting

$$Q^{-1}(f) = Q_0^{-1} f^{-a} \quad (8)$$

However, after evaluating the estimated error of Q^{-1} at each frequency point using bootstrapping, we found that the estimates for the low-frequency component (~1.5 Hz) of Q^{-1} were not stable. This may indicate that the focal mechanism or sediment layer affects the low-frequency amplitude of the seismic waveforms. Therefore, we only used the high frequency component (1.5 Hz ~ 20 Hz) of Q^{-1} to estimate Q_0^{-1} and a. Q_0^{-1} and a were estimated at 0.015 ± 0.007, 1.0 ± 0.02 respectively, with the least-square method (Figure 5-b).

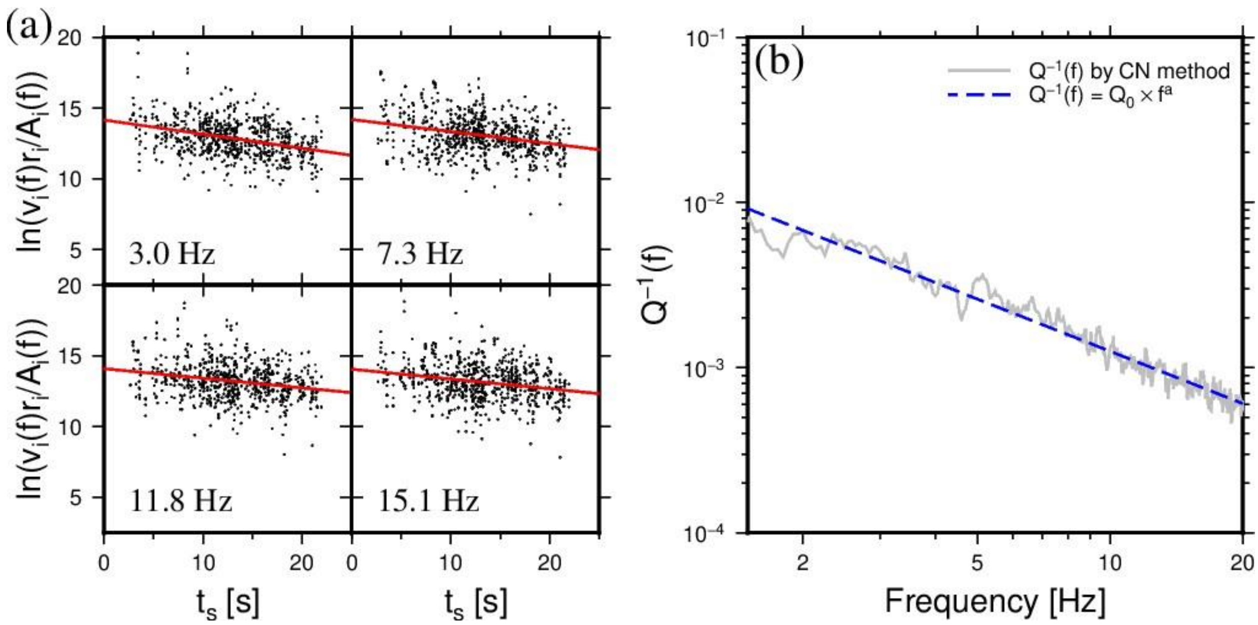

Figure 5. Estimated frequency-dependent attenuation factor Q^{-1} by coda normalization method. (a) The left-hand side of equation (7) versus direct S-wave travel-time t_{si} for four frequency points. The black dots indicate the individual data for each station and component for 14 earthquakes. The red line represents the best fit curve of equation (7). (b)

Estimated frequency-dependent Q^{-1}. The gray and blue dashed lines indicate the estimated Q^{-1} by coda normalization method and the best fit curve of equation (8), respectively.

2-5 Determination of source spectrum and quantification of scaled energy

2-5-1 Tentative estimation of the source spectrum

We tentatively determined the source spectrum for each earthquake using the site response and attenuation factors obtained in sections 2-3 and 2-4, according to equation (2). For each earthquake, the tentative source spectrum $S_0(f)$ was computed by correcting the site and path effects from the observed velocity spectra $v_i(f)$ for each station and component and taking their geometrical mean over the stations and components as follows:

$$S_0(f) = \frac{4\pi\rho\beta^3}{R_{\theta\phi}^{RMS}} \prod_{i=1}^{N} \left[\frac{v_i(f) r_i}{2\pi f G_i(f) F_{si} \exp\left(-\pi f t^*(f)\right)}\right]^{\frac{1}{N}} \tag{9}$$

where *N* denotes the number of velocity spectra used in the analysis. However, the site response factors estimated by the coda normalization method in section 2-3 are relative to those for the reference station. Therefore, we evaluated the site response factor for the reference station in the following section.

2-5-2 Site characteristic factor of the reference station

In section 2-3, we estimated the relative site response factors, assuming that the site response factor for the reference station is 1 for all frequency points for the three components. However, if the site response factor at reference station $G_0(f)$ deviated significantly from 1, the overall spectrum would deviate from the true one. In this study, we evaluated $G_0(f)$ based on the assumption that the logarithmic spectral residual of the tentative source spectrum $S_0(f)$ from the model source spectrum, assuming a Brune-type omega-square model (Brune, 1970) can represents the $G_0(f)$ (Figure 6-a and b) (Yoshida et al., 2017).

As in section 2-3 and 2-4, we used the 14 regular earthquakes because their rupture processes are simple, according to a previous study (Yoshida & Kanamori, 2023), thus, their source spectra are thought to be approximated by the omega-square model. We required the source corner frequencies and seismic moments to construct their model source spectra. For the seismic moments, we used the values listed in the F-net moment tensor catalog (NIED). We estimated the source corner frequencies of the 14 events based on the spectral ratio method using empirical Green's functions (EGFs). This method cancels site and path effects on the waveform by considering the spectral ratio of the earthquake to be suitable for a nearby smaller earthquake as an EGFs event (e.g., Mueller, 1985; Dreger, 1994). The detailed procedure of the spectral ratio method is described in Appendix A.

The gray lines in Figure 6-c represent the estimated G_0 values for the respective events. Of the 14 events, we estimated the source corner frequencies and obtained model source spectra for 11 events. We omitted three events because we could not find appropriate EGFs for them. The estimated $\log_{10} G_0(f)$ values decreased with increasing frequency. The similarity in the frequency characteristics of $G_0(f)$ values inferred from all 11 earthquakes that occurred at different locations supports the idea that the logarithmic spectral residuals of the tentative and model source spectrum represent the site response factor for the reference station. We used the geometric mean of $G_0(f)$ estimated from the 11 events as the representative value for subsequent analyses.

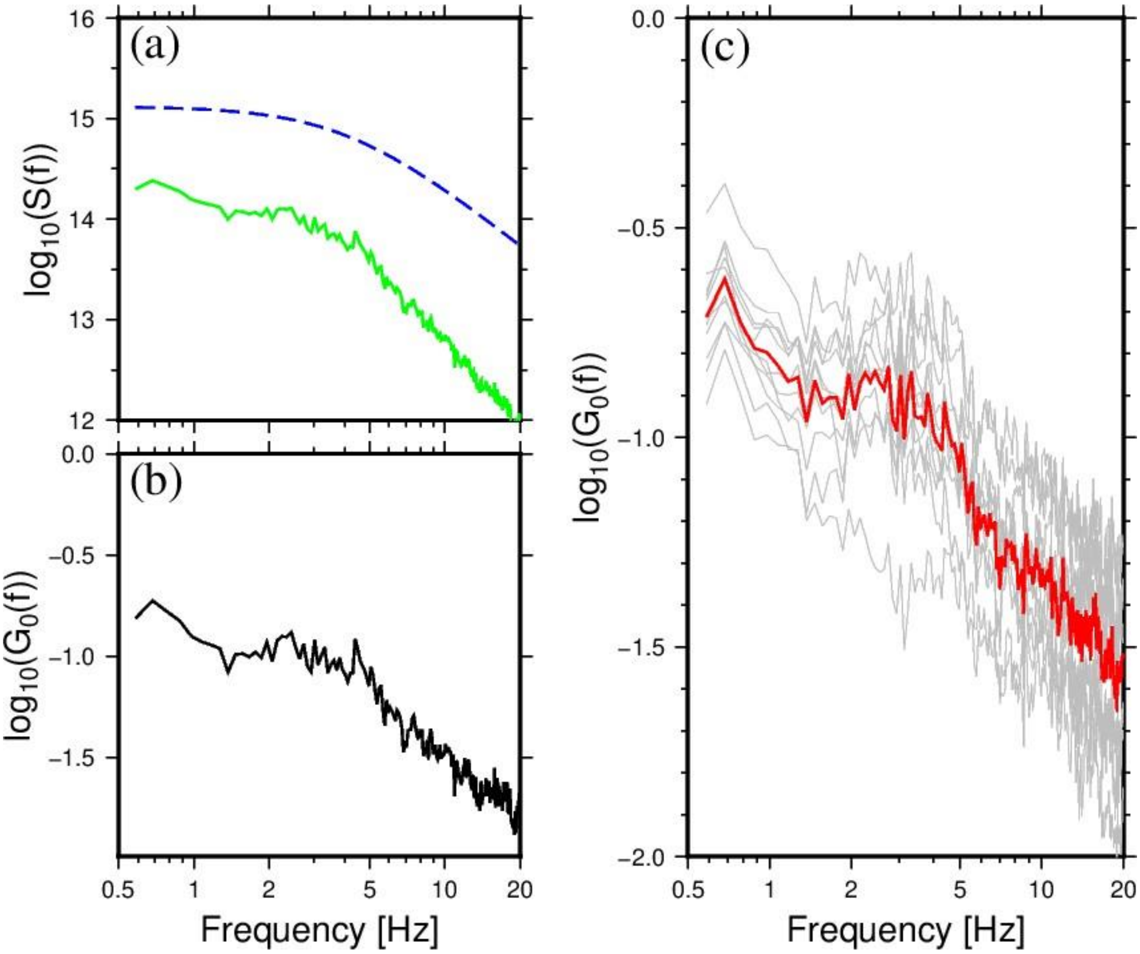

Figure 6. Estimated site response factor for the reference station $G_0(f)$. (a) Example of the model (blue dashed line) and estimated tentative source spectrum (green solid line). (b) The logarithmic spectra residual of the estimated tentative and model source spectrum (c) Estimated G_0. The gray and red lines represent the individual and average G_0, respectively.

2-5-3 Final estimation of source spectrum and scaled energy

Finally, we obtained the source spectrum $S(f)$ for each earthquake by correcting the site response factor for the reference station using the tentative source spectrum $S_0(f)$.

$$S(f) = \frac{S_0(f)}{G_0(f)} = \frac{4\pi\rho\beta^3}{G_0(f)R_{\theta\phi}^{RMS}} \times \prod_{i=1}^{N}\left[\frac{v_i(f)r_i}{2\pi f G_i(f) F_{si} \exp\left(-\pi f t^*(f)\right)}\right]^{\frac{1}{N}} \tag{10}$$

From the source spectrum estimated using equation (10), we calculated the seismic moment and radiated energy separately to obtain the scaled energy in equation (1). We determined the seismic moment (M_0) by fitting the model source spectrum (S_n^{cal}) to the derived source spectrum ($S(f)$) to minimize the residual ($|\log_{10} S(f) - \log_{10} S_n^{cal}(f)|$) (Figure 7);

$$S_n^{cal}(f) = \frac{M_0}{1 + (f/f_c)^n} \tag{11}$$

where f_c and n are the source corner frequency and spectral high-frequency falloff rate, respectively. We estimated f_c at 0.1 Hz intervals from 0.5 Hz to 20 Hz and n at 0.1 intervals from 0 to 4 with a grid-search method, respectively. Note that we did not use this result to calculate the radiated energy.

The radiated energy was calculated using the following equation (Vassiliou and Kanamori, 1982).

$$E_R = \frac{8\pi}{10\rho\beta^5}\int_0^\infty \left(fS(f)\right)^2 df \tag{12}$$

We ignored the P-wave radiated energy because most of the radiated energy was carried by S-wave (e.g., Kanamori et al., 2020). To calculate radiated energy based on equation (12), we used the derived source spectrum from 0.5 Hz to 20 Hz and extrapolated to the outside of the analyzed frequency band, assuming that the amplitude shows the value expected from the seismic moment for $f < 0.5$ Hz and decays in proportion to f^{-2} for $f > 20$ Hz, respectively (Snoke, 1987). It should be noted that we did not use the estimated n for extrapolation of the source spectrum and fixed the high-frequency falloff rate at 2 above 20 Hz because the falloff rate n estimated by fitting above did not represent a high-frequency falloff rate above 20 Hz, only up to 20 Hz. Finally, we determined the scaled energy for each earthquake in equation (1) using the radiated energy and seismic moment estimated above.

To evaluate the estimation uncertainty, we resampled individual source spectra at different stations and components by bootstrapping and calculated their geometric mean, estimated source corner frequency, high-frequency falloff rate, seismic moment, radiated energy, and scaled energy 200 times. Standard deviations calculated for each factor were used as measures of uncertainty.

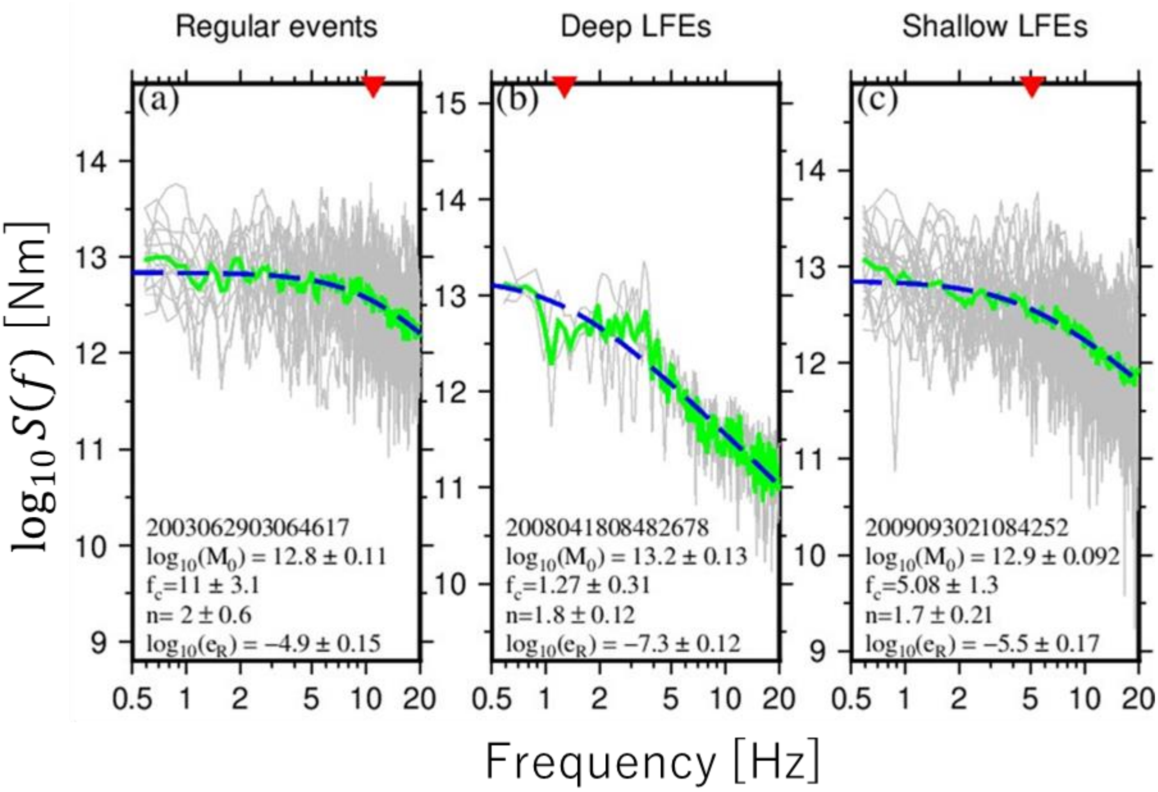

Figure 7. Examples of the estimated source spectra with the correction of the site response and attenuation factors. (a), (b), and (c) indicate source spectra for the regular earthquakes, the deep LFEs and the shallow LFEs, respectively. The gray lines indicate the individual source spectra from respective stations and components. The green solid and blue dashed lines indicate the geometric mean of the source spectra and the best-fit curve of equation (11), respectively. The red inverted triangles indicate the estimated source corner frequencies.

3 Results

We calculated the radiated energy (E_R) and seismic moment (M_0) using the derived source spectra and obtained the scaled energy (e_R) for 1464 regular earthquakes ($M_{jma} \geq 2.0$), 169 deep LFEs, and 52 shallow LFEs detected by Nakajima and Hasegawa (2021). Figure 8 shows the relationship between the moment magnitudes estimated in this study and those listed on the F-net moment tensor catalog (M_w^{NIED}) based on broadband data. We found a generally good agreement between them.

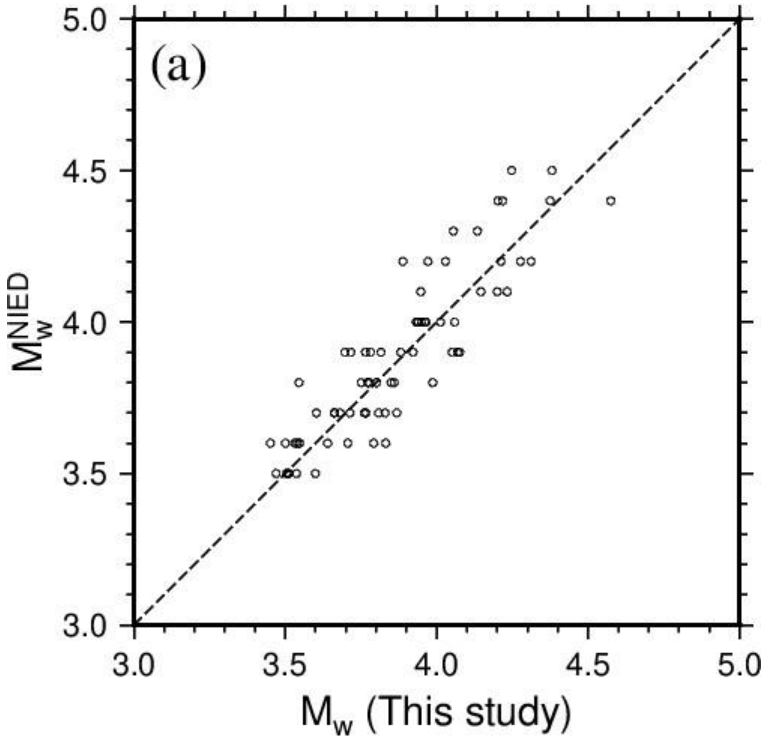

Figure 8. The relationship between moment magnitudes estimated in this study and those listed on F-net moment tensor catalog (M_w^{NIED}).

Figure 9-b shows the relationship between the estimated radiated energy and seismic moment. The radiated energy increased with seismic moment, and the radiated energy for LFEs was systematically lower than those for regular earthquakes with similar seismic moments (Figure 9-b).

Figure 9-a shows a histogram of the obtained e_R values and Figure 9-c shows e_R values as a function of the estimated moment magnitudes (M_w). The mean, standard error, and standard deviation of the estimated $\log_{10} e_R$ for regular earthquakes, deep, and shallow LFEs are shown in Table 1. For regular earthquakes, although e_R values are scattered, e_R values are on the order of 10^{-5}, which is consistent with previous studies on scaled energy for crustal earthquakes (e.g., Abercrombie,1995; Ide and Beroza, 2001; Prieto et al., 2004; Kanamori and Brodsky, 2004; Yoshida & Kanamori, 2023). On the other hand, the e_R values for the deep and shallow LFEs are on the order of 10^{-7} and 10^{-6}, respectively. This result indicates that e_R values for LFEs are one to three orders of magnitude lower than those for regular earthquakes.

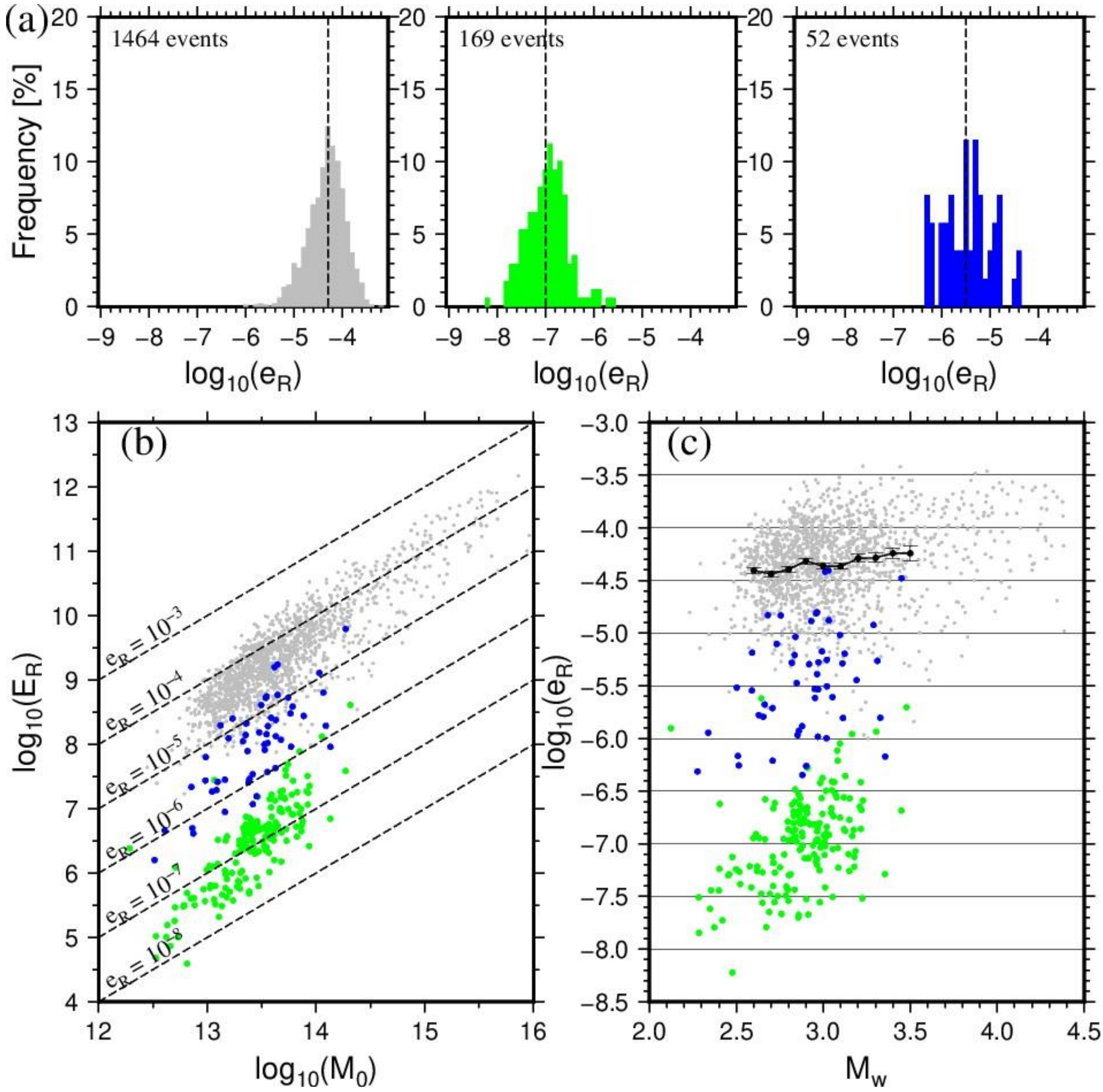

Figure 9. Estimated radiated energy (E_R), seismic moment (M_0) and scaled energy (e_R). (a) Histogram of e_R values. Gray, green, and blue histograms indicate the regular earthquakes ($M_{jma} \geq 2.0$), the deep and the shallow LFEs, respectively. (b) The relationship between the E_R values and M_0 values. (c) e_R values as a function of moment magnitudes (M_w) (Kanamori, 1977; Hanks and Kanamori, 1979). Gray, green, and blue circles indicate the regular earthquakes, deep and shallow LFEs, respectively. Black dots and error bars indicate the average e_R values and standard errors at 0.1 bins in the obtained M_w, respectively.

Table 1. Mean, standard deviation, and standard error of the obtained $\log_{10} e_R$

	Mean	Standard error	Standard deviation
The regular earthquakes	-4.29	0.02	0.39
The deep LFEs	-6.97	0.06	0.43
The shallow LFEs	-5.46	0.14	0.50

Scaled energy (e_R) is proportional to the product of stress drop ($\Delta\sigma$) and radiation efficiency (η) (e.g., Kanamori and Brodsky, 2004; Rivera and Kanamori, 2005) as,

$$e_R = \frac{\eta\Delta\sigma}{2\mu} \tag{13}$$

where μ is rigidity. Assuming that regular earthquakes and LFEs have the same radiation efficiency, the systematic difference in scaled energy indicates that the stress drops for LFEs are one to three orders of magnitude lower than those for regular earthquakes. For example, assuming that radiation efficiency is constant at 0.47 (e.g., Brune, 1970) and rigidity is constant at 30 GPa (e.g., Kanamori, 1977), average stress drops, based on our estimated mean scaled energy, are approximately 6.5 MPa, 0.013 MPa and 0.51 MPa for the regular earthquakes, deep, and shallow LFEs, respectively. However, for LFEs at plate boundaries, some studies have reported that not only the stress drop, but also the rupture velocity for LFEs is lower than that for regular earthquakes (e.g., Thomas et al., 2016; Supino et al., 2020). If LFEs are associated with slower rupture or deformation speeds than regular earthquakes, the radiation efficiency of LFEs should be lower than that of regular earthquakes (e.g., Venkataraman and Kanamori, 2004). In reality, LFEs are likely to exhibit a lower stress drop and radiation efficiency than regular earthquakes. Thus, our stress drop estimation based on the scaled energy yielded the minimum value of the stress drop for the LFEs.

Nakajima and Hasegawa (2021) detected shallow LFEs in this region based on the very low dominant frequencies of the observed direct S-waves compared to regular earthquakes with similar magnitudes. We showed that the e_R values of shallow LFEs are indeed systematically an order of magnitude smaller than those of regular earthquakes. However, it is uncertain whether shallow LFEs are essentially the same as deep LFEs or regular earthquakes with low dominant frequencies. Deep LFEs occur at distinctly greater depths than regular earthquakes and have different coda characteristics; however, the difference is not as obvious in the case of shallow LFEs versus regular earthquakes. To understand the source properties of shallow LFEs in more detail, it is necessary to investigate not only direct S-waves but also the characteristics of coda waves and their focal mechanisms (Yoshida et al., 2020).

4. Discussion

4.1 The effect of assuming the homogenous attenuation factor and setting a time window on e_R for deep LFEs

We determined the attenuation factor Q^{-1} in section 2-3 assuming a spatially homogeneous Q^{-1} in and around the focal area of the 2008 Iwate-Miyagi earthquake. However, deep LFEs occur at greater depths (20–30 km) than regular earthquakes (10 km). Thus, the representative attenuation factor Q^{-1} for deep LFEs may differ from that for regular earthquakes, which may lead to a systematic bias in the estimation of the source spectra and scaled energy for deep LFEs. To evaluate the effect of the depth variation in the attenuation factor Q^{-1} on e_R for the deep LFEs, we tested a case with a two-layer structure of Q^{-1} bounded at a depth of 15 km. We compared e_R values assuming this model to e_R

values assuming the spatially homogeneous Q^{-1} structure. We considered the following two structures using an attenuation factor Q^{-1} at 1 Hz (Q_0^{-1}):

Model 1. Deep Q^{-1} is larger than shallow Q^{-1}

$$Q_0^{-1} = \begin{cases} 0.015 \ \ (\text{shallower than } 15 \text{ km}) \\ 0.025 \ \ (\text{deeper than } 15 \text{ km}) \end{cases}$$

Model 2. Deep Q^{-1} is smaller than shallow Q^{-1}.

$$Q_0^{-1} = \begin{cases} 0.015 \ \ (\text{shallower than } 15 \text{ km}) \\ 0.010 \ \ (\text{deeper than } 15 \text{ km}) \end{cases}$$

For the values of the frequency-dependent factor (a) and shallower Q_0^{-1}, we used the values estimated by the coda normalization method in section 2-4. The value of Q_0^{-1} for the deeper part of model 1 was determined based on the seismic attenuation structure beneath northeastern Japan, as estimated by Nakajima et al. (2013).

Figure 10 shows the difference between $\log_{10} e_R$ assuming each model and $\log_{10} e_R$ assuming the spatially homogeneous Q^{-1}. For model 1, the differences in $\log_{10} e_R$ for the regular earthquakes and shallow LFEs that occurred in the upper crust were almost 0, and only approximately 0.1 to 0.2 for the deep LFEs. For model 2, the difference in $\log_{10} e_R$ between the regular earthquakes and shallow LFEs was approximately 0 and -0.1 for the deep LFEs. This result suggests that the difference in $\log_{10} e_R$ between regular earthquakes and LFEs was not due to the depth variation in Q^{-1}.

Another feature of deep LFEs is that they have a longer duration of seismic waves than regular earthquakes of a similar magnitude (e.g., Ukawa and Ohtake, 1987; Hasegawa and Yamamoto, 1994). The length of the time window may also affect the scaled energy estimates for deep LFEs. To investigate the effects of the time window, we estimated the scaled energy using different time window lengths (10.24 s) and compared them with those based on the original time window length (3.3 s). For comparison, we used only the observed spectra that met the SNR conditions described in section 2-2 in both time windows. Figure 11 shows the difference in $\log_{10} e_R$ using a 10.24 s and original time-window length. The difference in $\log_{10} e_R$ was only approximately 0.6, which suggests that the effect of time-window length is not large enough to explain the difference in the scaled energy between the regular earthquakes and the LFEs. These results suggest that the systematic difference in scaled energy between regular earthquakes and LFEs is not due to the depth variation in Q^{-1} or an inappropriate setting of the time window.

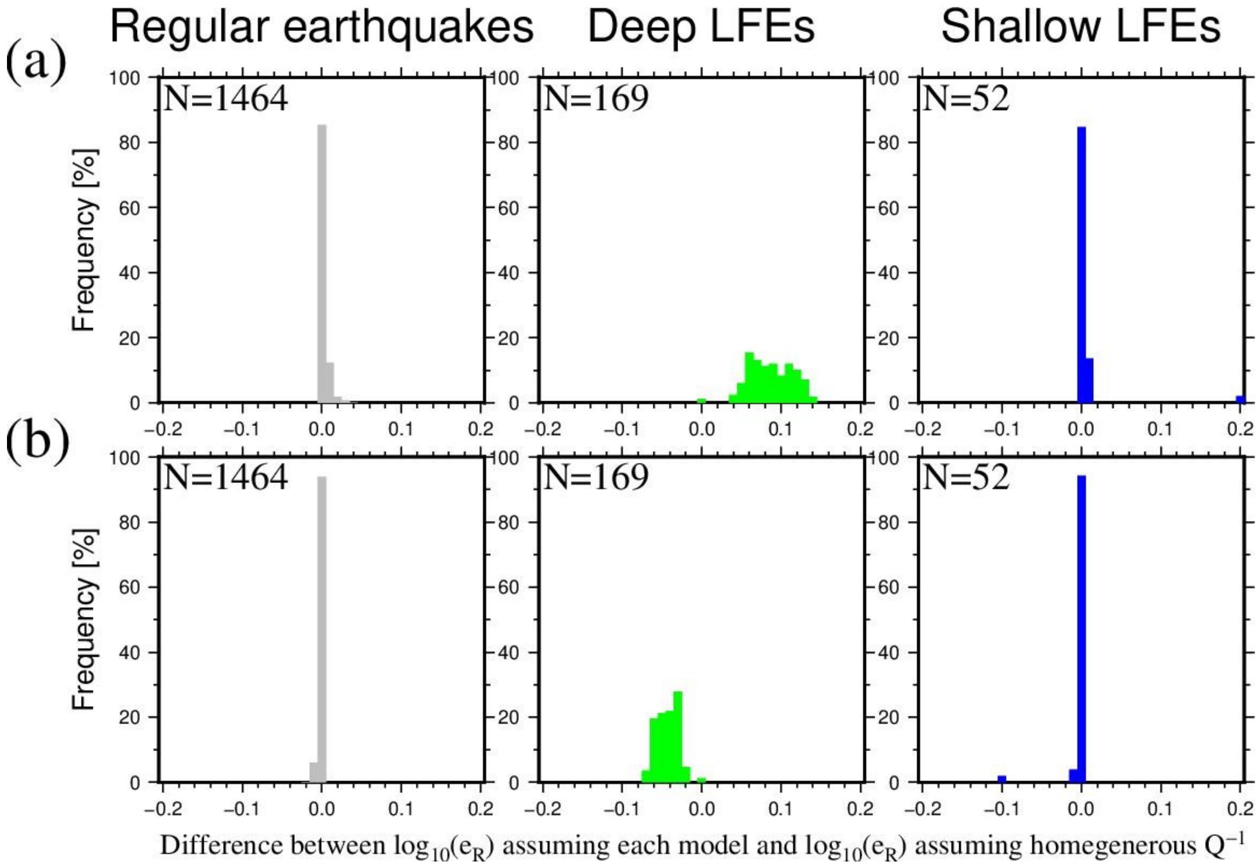

Figure 10. Difference in $\log_{10} e_R$ obtained from a two-layered Q^{-1} model (a: Model 1, b: Model 2) and from the spatially homogeneous Q^{-1} model. Gray, green, and blue histograms indicate the regular earthquakes, deep, and shallow LFEs, respectively.

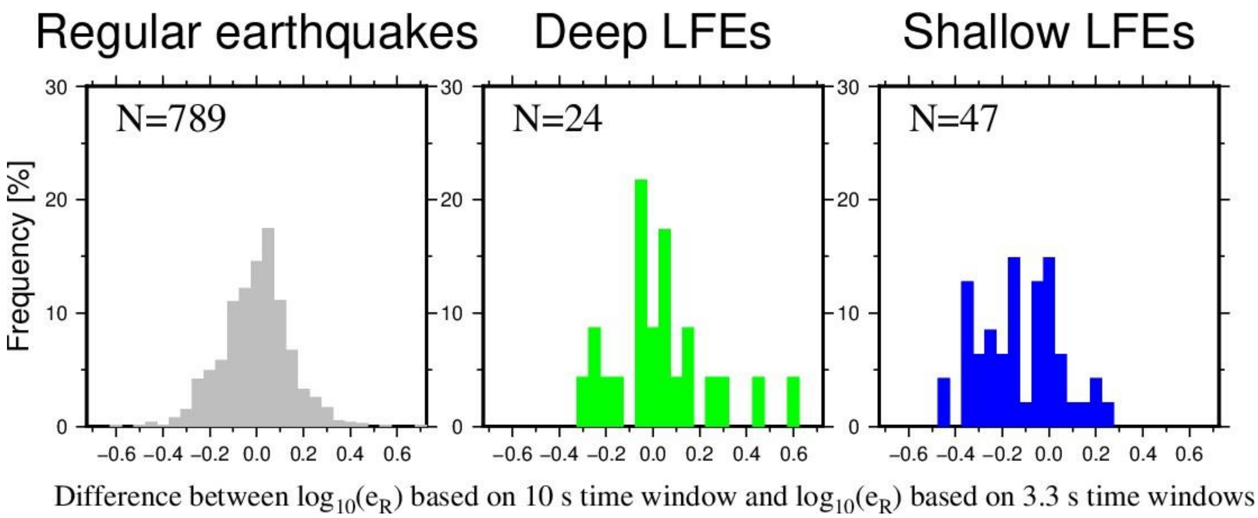

Figure 11. Difference in $\log_{10} e_R$ using two different time windows (3.3 s and 10.24 s). (a), (b), and (c) indicate the result of the regular earthquakes, deep and shallow LFEs, respectively.

4.2 Depth and spatial distribution of scaled energy for the regular earthquakes

As shown in Figure 9, we found that the scaled energy (e_R) for regular earthquakes was in the order of 10^{-5} to 10^{-4}. However, the estimated e_R values for the regular earthquakes were scattered. To evaluate the diversity of e_R values among regular earthquakes, we investigated the depth and spatial variation of e_R values. Figure 12 shows e_R values plotted against focal depth. Although we considered the depth variation of the seismic wave velocity in estimating e_R values, the values obtained for regular earthquakes tended to increase with the focal depth. For regular earthquakes, previous studies have suggested that stress drops tend to increase with focal depth (e.g., Hardebeck and Aron, 2009; Boyd et al., 2017; Huang et al., 2017; Trugman, 2020). Assuming that the radiation efficiency is constant for all regular earthquakes, the scaled energy is proportional to the stress drop (e.g., Kanamori and Brodsky, 2004; Rivera and Kanamori, 2005). The obtained depth-dependent tendency may indicate that the stress drops increase with focal depth. In contrast, some studies attributed the focal depth dependence of stress drop to the assumption of a spatially homogeneous attenuation factor Q^{-1} (e.g., Abercrombie et al., 2021). In section 4-1, we showed that the systematic difference in e_R values between regular earthquakes and deep LFEs is not due to the depth variation of Q^{-1} using two-layer structures of Q^{-1}. However, because the seismic attenuation Q^{-1} structure in the upper crust in and around the focal area of the 2008 Iwate-Miyagi earthquake is not well-constrained, we cannot rule out the possibility that the weak focal depth dependence of the obtained e_R values is due to the assumption of a spatially homogeneous Q^{-1} structure in the upper crust. Hereafter, for regular earthquakes, we compared e_R values only for earthquakes that occurred at similar depths. Unlike regular earthquakes, e_R values for deep LFEs exhibit no clear depth dependence.

Figure 13 shows the spatial distribution of e_R values for the regular earthquakes and as a function of distance from the nearest volcanoes. Although e_R values are scattered, they tend to decrease with decreasing distance from the nearest volcanoes (Figure 13-c) and tend to be small, close to the shallow LFEs (Figure 13-a, b). Low seismic wave velocities (Okada et al., 2010) and relatively high pore pressure ratio regions (Yoshida et al., 2014b) were estimated beneath the volcanoes in and around the aftershock areas of the 2008 Iwate-Miyagi earthquakes. Crustal fluids and high pore pressures may be related to the diversity of e_R values between regular earthquakes. Some studies have indicated that the stress drop decreases when the frictional strength decreases owing to the fluid and high pore pressure (e.g., Goertz-Allmann et al., 2011b; Kwiatek et al., 2014; Yoshida et al., 2017). In addition, fluid and high pore pressure may affect rupture and slip velocity (e.g., Liu and Rice, 2005). These effects may be related to regular earthquakes with relatively small e_R values. However, because we do not know the detailed spatial variation of the seismic attenuation factor Q^{-1} in the upper crust, we cannot rule out the possibility that near-source attenuation due to crustal fluid contributes to regular earthquakes with relatively low e_R values. In both cases, this result suggests that we can obtain information regarding the presence of fluid or near-source medium properties through the spectral analysis of seismic waves.

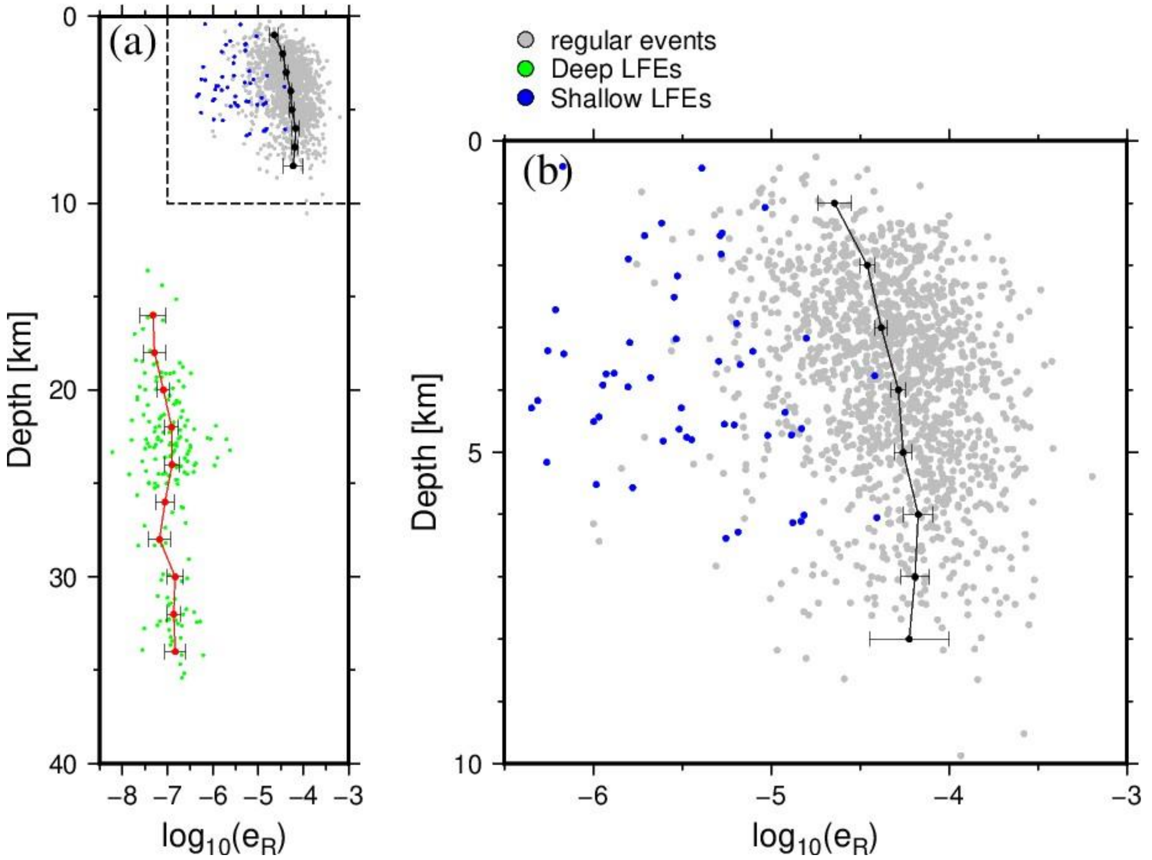

Figure 12. The obtained e_R values as a function of focal depths. (a) Shallower than 40 km. (b) In the dashed rectangle in (a), gray, green, and blue circles indicate the regular earthquakes, deep and shallow LFEs, respectively. The black dots and error bars show the average e_R values and standard error of the regular earthquakes for each depth range of 1 km. The red dots and error bars indicate the average e_R values and standard errors of the deep LFEs for each 2 km depth range.

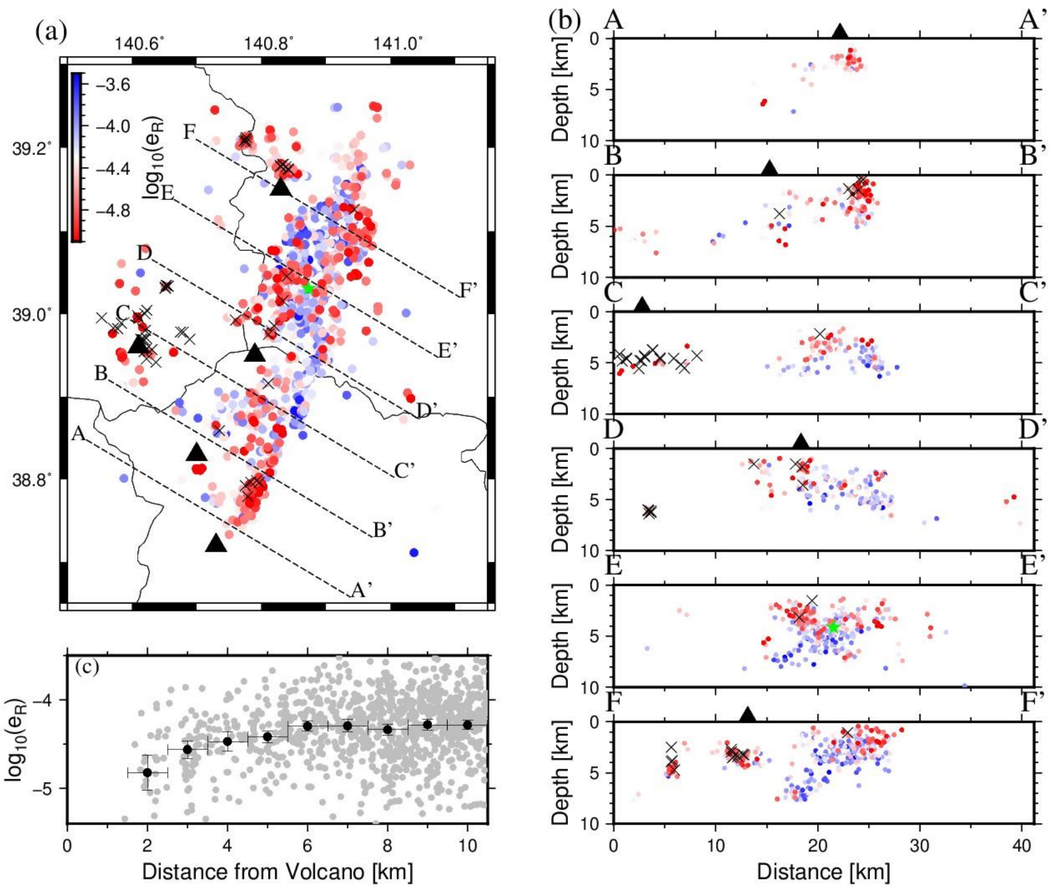

Figure 13. Spatial distribution of the regular earthquakes colored by e_R values. (a) Map view. (b) Cross-sectional views along lines A–A' to F–F' in (a). Circle colored by e_R values and cross marks indicate the regular earthquakes and the shallow LFEs, respectively. Black triangles indicate volcanoes. The green star indicates the 2008 Iwate-Miyagi earthquake. (c) e_R values plotted against the distance from the nearest volcano. Gray dots indicate individual data. Black dots and error bars indicate e_R values and standard errors in the range of 1 km.

4.3. Comparison of the seismic moment and radiated energy between the regular earthquakes and the LFEs

In this study, we estimated the seismic moments for LFEs based on source spectra using a good observation network. Owing to the absence of such a good observational network, we could not estimate the seismic moment, and the only available measure of the LFE size was the local magnitude. In this study, we investigated the relationship between the radiated energy, seismic moment, and local magnitude (M_{jma}). M_{jma} is a magnitude scale based on the maximum amplitude of the seismic waveform determined by the JMA (Katsumata, 1999, 2004).

To compare M_{jma} and moment magnitude (M_w) for a wider magnitude range, in addition to the results of the regular earthquakes with $M_{jma} \geq 2.0$ obtained in section 3, we estimated M_w for 13619 regular earthquakes with $1.0 \leq M_{jma} \leq 1.9$ in and around the focal area of the 2008 Iwate-Miyagi earthquake. Because the SNRs at the low-frequency component (< 5 Hz) are not high for small earthquakes, we used the observed velocity spectra from 5 Hz to 20 Hz to estimate moment magnitudes for regular earthquakes with

$1.0 \leq M_{jma} \leq 1.9$. Figure 14-a shows the relationship between M_{jma} and M_w. M_w tended to be greater than M_{jma} for all three types of earthquakes: regular earthquakes ($M_{jma} < 3.5$), deep LFEs, and shallow LFEs. However, the discrepancy between M_w and M_{jma} for the LFEs was larger than that for the regular earthquakes.

Some previous studies indicated that M_w for regular earthquakes with $M_L < 4$ (M_L indicates local magnitude) tends to be larger than M_L (e.g., Grünthal & Wahlström, 2003; Edwards et al., 2010; Goertz-Allmann et al., 2011a; Munafò et al., 2016; Ross et al., 2016; Uchide and Imanishi, 2018). Our results are consistent with these previous studies. We evaluated the approximate relationship between M_w and M_{jma} for small regular earthquakes with $1.0 \leq M_{jma} \leq 4.0$. Because it does not appear to have a linear relationship, we assumed the form of $M_w = aM_{jma}^2 + bM_{jma} + c$. We obtained $a = 0.49 \pm 0.03$, $b = 0.35 \pm 0.01$ and $c = 1.65 \pm 0.03$, respectively, which fits the observation well (Figure 14-a), by the least-square method.

We estimated the energy magnitude (M_E), defined as $M_E = (\log_{10} E_R - 4.8)/1.5$ (Choy and Boatwright, 1995) using the radiated energy (E_R) [unit: J]. Figure 14-b shows the relationship between M_{jma} and M_E. Although the obtained M_E values are scattered, we found generally good agreement between M_{jma} and M_E for the three types of earthquakes. The observed nonlinear relationship between M_w and M_{jma}, on the other hand, may indicate that M_{jma} based on the maximum amplitude of seismic waves, reflects the radiated energy rather than the seismic moment. The obtained M_w of LFEs is significantly larger than M_{jma} because LFEs radiate less energy than regular earthquakes with similar seismic moments, as indicated by e_R.

Figure 14-c shows the relationship between M_w and M_E. For regular earthquakes, M_w and M_E showed good agreement. On the other hand, for the LFEs, M_w was 1–2, which was systematically larger than M_E. This trend can be understood by the difference in the scaled energy between regular earthquakes and LFEs. We can write the $M_w - M_E$ relationship with e_R (Choy and Boatwright, 1995) as follows:

$$M_w - M_E = -\frac{2}{3}(\log e_R + 4.3) \quad (14)$$

Equation (14) indicates that M_w is equal to M_E when e_R value is approximately 5×10^{-5} and the discrepancy between M_E and M_w increases as e_R values decrease. The generally good agreement between M_w and M_E for the regular earthquakes reflect that e_R values for regular earthquakes are in the order of 10^{-5} to 10^{-4} as shown in Figure 9. This is reasonable because Kanamori (1977) originally defined M_w to satisfy the Gutenberg-Richter magnitude-energy relation (Gutenberg, 1956) assuming e_R values to be approximately 5×10^{-5}. However, the large discrepancy in the LFEs may reflect the fact that the e_R values of the LFEs is systematically one to three orders of magnitude smaller than those of regular earthquakes. This result suggests that for LFEs, the local magnitude may provide relatively good information for the radiated energy but not for the seismic moment.

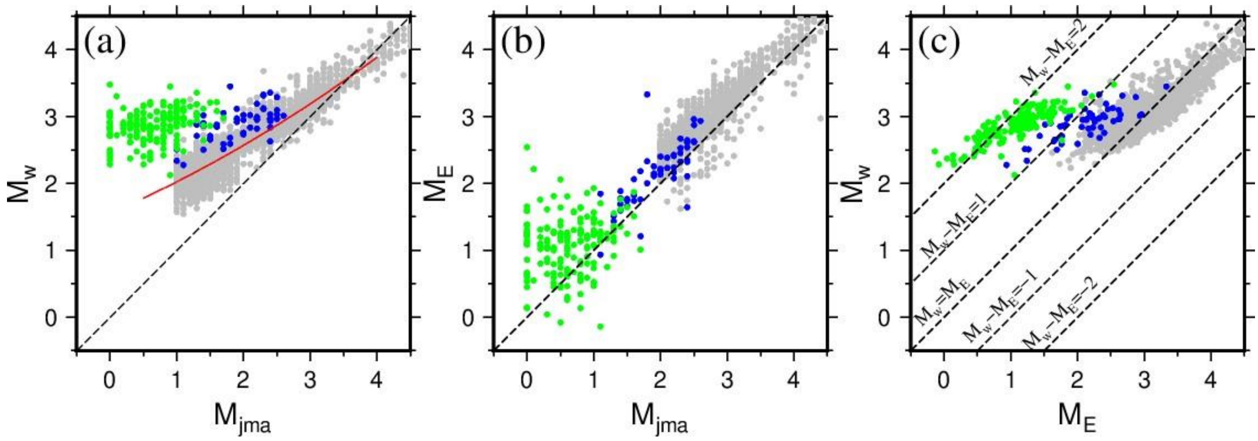

Figure 14. The estimated moment magnitude (M_w) and energy magnitude (M_E). (a) M_w as a function of M_{jma}. The red line indicates the best fit curve of $M_w = aM_{jma}^2 + bM_{jma} + c$. (b) M_E as a function of M_{jma}. (c) M_w as a function of M_E. Gray, green, and blue circles indicate the regular earthquakes, deep and shallow LFEs, respectively.

4.4. Spectral high-frequency falloff rate n as a clue to source complexity

Finally, the frequency characteristics of the derived source spectra were investigated. This section focuses on the high-frequency spectral falloff rate (n) estimated in section 2-5-3. Because of the narrow frequency band, we could not estimate n values stably for earthquakes whose estimated corner frequencies were larger than 10 Hz. Thus, we evaluated only n values for the earthquakes with estimated corner frequencies lower than 10 Hz. We estimated n values for 844 regular earthquakes, 169 deep LFEs, and 52 shallow LFEs. Figure 15 shows the histograms of the estimated n values and Table 2 shows the mean, standard error, and standard deviation of the obtained n values. For regular earthquakes, the mean values of obtained n was 1.61, which was smaller than the value of n assumed in the omega-square model ($n = 2$). Previous studies reported the existence of regular earthquakes with n < 2 (e.g., Allmann and Shearer, 2009; Trugman and Shearer, 2017; Shearer et al., 2022). The mean n value in this study was similar to that reported by Allmann and Shearer (2009). For earthquakes associated with complex fault ruptures such as multiple shock, the frequency-characteristic of source spectrum becomes more complex, deviating from the ω^2 model (e.g., Madariaga, 1979) and high-frequency energy radiation increases, which may be related to the smaller n values compared with the ω^2 model. Because of the presence of earthquakes associated with complex rupture processes, the average n values for regular earthquakes may be less than two.

In contrast, the mean values of the obtained n is 1.34 for 169 deep LFEs, and is 1.41 for 52 shallow LFEs. Thus, LFEs tend to have smaller n values than regular earthquakes, which is consistent with previous studies on LFEs at plate boundaries (e.g., Ide et al., 2007a) and continental plates (e.g., Yoshida et al., 2020). However, it should be noted that n values must be greater than 1.5 because the radiated energy defined by equation (12) diverges to infinity if $n \leq 1.5$. Thus, the estimated n v values smaller than 1.5 for the LFEs probably represent the characteristics of the source spectrum for a limited frequency band.

Compared to regular earthquakes, the average n values for the LFEs are smaller, which may suggest that the difference in frequency characteristics between regular earthquakes and LFEs results from not only the source corner frequency but also the spectral high-frequency falloff rate above the corner frequency. The smaller n values for the LFEs are seemingly inconsistent with their smaller radiated energy. However, the source corner frequencies of the LFEs were lower than those of regular earthquakes with similar magnitudes. Our results suggest that the high-frequency energy of LFEs is small owing to the small corner frequency, probably due to lower slip and/or deformation rates compared with regular earthquakes, rather than n value. Previous studies have suggested that deep LFEs may be related to multiple subevents such as a chain of tensile-shear cracks (Ikegaya and Yamamoto, 2021) and fluid resonance after shear faulting (Hensch et al., 2019). The systematically smaller n values for the LFEs suggest that LFEs are composed of complex rupture and/or deformation processes that radiate multiple low-frequency pulses. However, it should be noted that the upper limit of the currently available frequency band in this study is 20 Hz; therefore, the complexity of the spectrum on the high-frequency side becomes more distinct for events with a smaller source corner frequency (f_c) (Figure B-1).

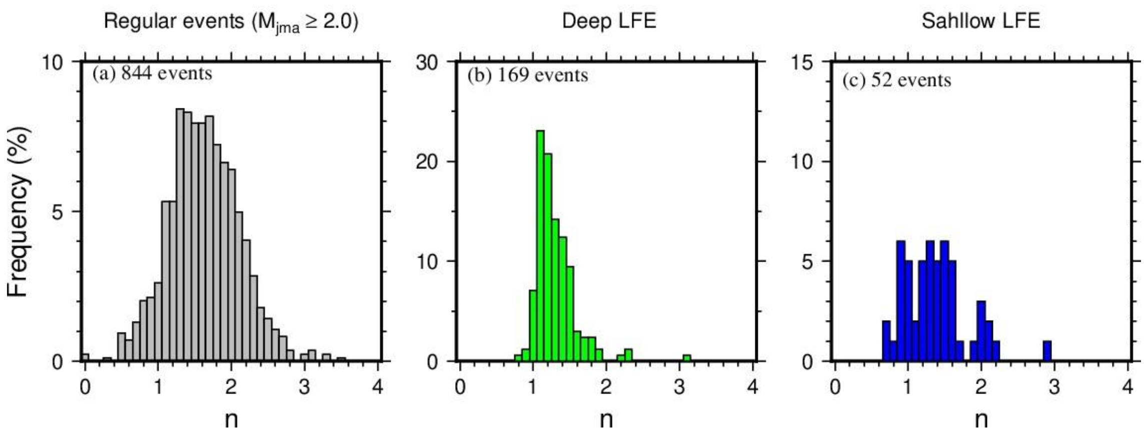

Figure 15. Estimated spectral high-frequency falloff rate n. (a), (b), and (c) indicate the histogram of the obtained n for the regular earthquakes, deep, and shallow LFEs, respectively.

Table 2. Mean, standard error and standard deviation of the obtained n

	Mean	Standard error	Standard deviation
The regular earthquakes	1.61	0.02	0.49
The deep LFEs	1.34	0.08	0.28
The shallow LFEs	1.41	0.10	0.43

5. Conclusion

In this study, we estimated the source spectra and obtained the scaled energy for 1469 regular earthquakes with $M_{jma} \geq 2.0$, 169 deep LFEs, and 52 shallow LFEs detected by Nakajima and Hasegawa (2021) in and around the focal area of the 2008 M_w 6.9 Iwate-Miyagi earthquake. The scaled energy (e_R) for regular earthquakes are in the order of 10^{-5} to 10^{-4}, which is consistent with previous studies. Additionally, our results show that regular earthquakes with relatively smaller e_R tend to occur near volcanoes and close to the location of shallow LFEs, suggesting that crustal fluid may be related to seismic radiation. On the other hand, e_R is of the order of 10^{-7} for deep LFEs, and 10^{-6} for shallow LFEs. The obtained systematic difference did not change even if accounting for the depth variation of the attenuation factor Q^{-1}. In addition, the spectral high-frequency falloff rates for LFEs tended to be lower than those for regular earthquakes. These results suggest that LFEs are associated with complex rupture and/or deformation processes with lower stress drops and/or slower rupture and/or deformation rates than those of regular earthquakes.

Although we found generally good agreement between the local magnitudes and energy magnitudes derived from the radiated energy for the three types of earthquakes, the discrepancy between the local magnitudes and moment magnitudes was significantly large for the LFEs. This result suggests that for LFEs, the local magnitude provides relatively good information about the radiated energy but does not provide information about the seismic moment.

Acknowledgment

The waveform data used in this study were provided by Hi-net (the National Research Institute for Erath and Science and Disaster Resilience), Japan Meteorological Agency, and Tohoku University. M.O. thanks Mare Yamamoto for comments and discussions on the LFEs. All figures in this study were created using GMT (Wessel and Smith, 1998)

References

Abercrombie, R. E. (1995). Earthquake source scaling relationships from −1 to 5 M_L using seismograms recorded at 2.5-km depth. *Journal of Geophysical Research: Solid Earth*, *100*(B12), 24015–24036. https://doi.org/10.1029/95JB02397

Abercrombie, R. E., Trugman, D. T., Shearer, P. M., Chen, X., Zhang, J., Pennington, C. N., Hardebeck, J. L., Goebel, T. H. W., & Ruhl, C. J. (2021). Does Earthquake Stress Drop Increase With Depth in the Crust? *Journal of Geophysical Research: Solid Earth*, *126*(10), 1–22. https://doi.org/10.1029/2021JB022314

Aki, K. (1967). Scaling law of seismic spectrum. *Journal of Geophysical Research*, *72*(4), 1217–1231. https://doi.org/10.1029/jz072i004p01217

Aki, K. (1980). Attenuation of shear-waves in the lithosphere for frequencies from 0.05 to 25 Hz. *Physics of the Earth and Planetary Interiors*, *21*(1), 50–60. https://doi.org/10.1016/0031-9201(80)90019-9

Aki, K., & Chouet, B. (1975). *Origin of Coda Waves : Source , Attenuation , and Scattering Effects earthquake at Norsar near*. *80*(23), 3322–3342.

Aki, K., Fehler, M., & Das, S. (1977). Source mechanism of volcanic tremor: fluid-driven crack models and their application to the 1963 kilauea eruption. *Journal of Volcanology and Geothermal Research*, *2*(3), 259–287. https://doi.org/10.1016/0377-0273(77)90003-8

Aki, K., & Koyanagi, R. (1981). Deep volcanic tremor and magma ascent mechanism under Kilauea, Hawaii. *Journal of Geophysical Research*, *86*(B8), 7095. https://doi.org/10.1029/JB086iB08p07095

Allmann, B. P., & Shearer, P. M. (2009). Global variations of stress drop for moderate to large earthquakes. *Journal of Geophysical Research: Solid Earth*, *114*(1), 1–22. https://doi.org/10.1029/2008JB005821

Aso, N., & Ide, S. (2014). Focal mechanisms of deep low-frequency earthquakes in Eastern Shimane in Western Japan. *Journal of Geophysical Research: Solid Earth*, *119*(1), 364–377. https://doi.org/10.1002/2013JB010681

Aso, N., Ohta, K., & Ide, S. (2013). Tectonic, volcanic, and semi-volcanic deep low-frequency earthquakes in western Japan. *Tectonophysics*, *600*, 27–40. https://doi.org/10.1016/j.tecto.2012.12.015

Aso, N., & Tsai, V. C. (2014). Cooling magma model for deep volcanic long-period earthquakes. *Journal of Geophysical Research: Solid Earth*, *119*(11), 8442–8456. https://doi.org/10.1002/2014JB011180

Baltay, A., Ide, S., Prieto, G., & Beroza, G. (2011). Variability in earthquake stress drop and apparent stress. *Geophysical Research Letters*, *38*(6). https://doi.org/10.1029/2011GL046698

Boyd, O. S., McNamara, D. E., Hartzell, S., & Choy, G. (2017). Influence of Lithostatic Stress on Earthquake Stress Drops in North America. *Bulletin of the Seismological Society of America*, *107*(2), 856–868. https://doi.org/10.1785/0120160219

Brune, J. N. (1970). Tectonic stress and the spectra of seismic shear waves from earthquakes. *Journal of Geophysical Research*, *75*(26), 4997–5009. https://doi.org/10.1029/JB075i026p04997

Choy, G. L., & Boatwright, J. L. (1995). Global patterns of radiated seismic energy and apparent stress. *Journal of Geophysical Research*, *100*(B9). https://doi.org/10.1029/95jb01969

Dreger, D. S. (1994). Empirical Green's function study of the January 17, 1994 Northridge, California earthquake. *Geophysical Research Letters*, *21*(24), 2633–2636. https://doi.org/10.1029/94GL02661

Edwards, B., Allmann, B., Fäh, D., & Clinton, J. (2010). Automatic computation of moment magnitudes for small earthquakes and the scaling of local to moment magnitude. *Geophysical Journal International*, *183*(1), 407–420. https://doi.org/10.1111/j.1365-246X.2010.04743.x

Goertz-Allmann, B. P., Edwards, B., Bethmann, F., Deichmann, N., Clinton, J., Fah, D., & Giardini, D. (2011)a. A New Empirical Magnitude Scaling Relation for Switzerland. *Bulletin of the Seismological Society of America*, *101*(6), 3088–3095. https://doi.org/10.1785/0120100291

Goertz-Allmann, B. P., Goertz, A., & Wiemer, S. (2011)b. Stress drop variations of induced earthquakes at the Basel geothermal site. *Geophysical Research Letters*, *38*(9), 2011GL047498. https://doi.org/10.1029/2011GL047498

Grünthal, G., & Wahlström, R. (2003). An Mw based earthquake catalogue for central, northern and northwestern Europe using a hierarchy of magnitude conversions. *Journal of Seismology*, *7*(4), 507–531. https://doi.org/10.1023/B:JOSE.0000005715.87363.13/METRICS

Gutenberg, B. (1956). The energy of earthquakes. *Quarterly Journal of the Geological Society of London*, *112*(1–4), 1–14. https://doi.org/10.1144/GSL.JGS.1956.112.01-04.02

Hanks, T. C., & Kanamori, H. (1979). A moment magnitude scale. *Journal of Geophysical Research: Solid Earth*, *84*(B5), 2348–2350. https://doi.org/10.1029/JB084IB05P02348

Hardebeck, J. L., & Aron, A. (2009). Earthquake Stress Drops and Inferred Fault Strength on the Hayward Fault, East San Francisco Bay, California. *Bulletin of the Seismological Society of America*, *99*(3), 1801–1814. https://doi.org/10.1785/0120080242

Hasegawa, A., Zhao, D., Hori, S., Yamamoto, A., & S Horiuchi. (1991). Deep structure of the northeastern Japan arc and its relationship to seismic and volcanic activity. *Nature*, *352*, 683–689. https://www.nature.com/articles/352683a0

Hasegawa, A., & Nakajima, J. (2022). Low-frequency Earthquakes in the Continental Plate and Their Seismological and Tectonic Implications. *Journal of Geography (Chigaku Zasshi)*, *131*(3), 289–315. https://doi.org/10.5026/jgeography.131.289

Hasegawa, A., Nakajima, J., Umino, N., & Miura, S. (2005). Deep structure of the northeastern Japan arc and its implications for crustal deformation and shallow seismic activity. *Tectonophysics*, *403*(1–4), 59–75. https://doi.org/10.1016/j.tecto.2005.03.018

Hasegawa, A., & Yamamoto, A. (1994). Deep, low-frequency microearthquakes in or around seismic low-velocity zones beneath active volcanoes in northeastern Japan. *Tectonophysics*, *233*(3–4), 233–252. https://doi.org/10.1016/0040-1951(94)90243-7

Hensch, M., Dahm, T., Ritter, J., Heimann, S., Schmidt, B., Stange, S., & Lehmann, K. (2019). Deep low-frequency earthquakes reveal ongoing magmatic recharge beneath Laacher See Volcano (Eifel, Germany). *Geophysical Journal International*, *216*(3), 2025–2036. https://doi.org/10.1093/gji/ggy532

Huang, Y., Ellsworth, W. L., & Beroza, G. C. (2017). Stress drops of induced and tectonic earthquakes in the central United States are indistinguishable. *Science Advances*, *3*(8). https://doi.org/10.1126/SCIADV.1700772

Ide, S., & Beroza, G. C. (2001). Does apparent stress vary with earthquake size? *Geophysical Research Letters*, *28*(17), 3349–3352. https://doi.org/10.1029/2001GL013106

Ide, S., Beroza, G. C., Shelly, D. R., & Uchide, T. (2007)a. A scaling law for slow earthquakes. *Nature*, *447*(7140), 76–79. https://doi.org/10.1038/nature05780

Ide, S., Shelly, D. R., & Beroza, G. C. (2007)b. Mechanism of deep low frequency earthquakes: Further evidence that deep non-volcanic tremor is generated by shear slip on the plate interface. *Geophysical Research Letters*, *34*(3). https://doi.org/10.1029/2006GL028890

Ikegaya, T., & Yamamoto, M. (2021). Spatio-temporal characteristics and focal mechanisms of deep low-frequency earthquakes beneath the Zao volcano, northeastern Japan. *Journal of Volcanology and Geothermal Research*, *417*, 107321. https://doi.org/10.1016/j.jvolgeores.2021.107321

Julian, B. R. (1994). Volcanic tremor: Nonlinear excitation by fluid flow. *Journal of Geophysical Research: Solid Earth*, *99*(B6), 11859–11877. https://doi.org/10.1029/93JB03129

Kamaya, N., & Katsumata, A. (2004). Low-frequency Events away from Volcanoes in the Japan Islands. *Zisin (Journal of the Seismological Society of Japan. 2nd Ser.)*, *57*(1), 11–28. https://doi.org/10.4294/ZISIN1948.57.1_11

Kanamori, H. (1977). The energy release in great earthquakes. *Journal of Geophysical Research*, *82*(20), 2981–2987. https://doi.org/10.1029/JB082i020p02981

Kanamori, H., & Brodsky, E. E. (2004). The physics of earthquakes. *Reports on Progress in Physics*, *67*(8), 1429–1496. https://doi.org/10.1088/0034-4885/67/8/R03

Kanamori, H., Mori, J., Hauksson, E., Heaton, T. H., Hutton, L. K., & Jones, L. M. (1993). Determination of earthquake energy release and M_L using TERRAscope. Bulletin of the Seismological Society of America, *83*(2), 330–346. https://doi.org/https://doi.org/10.1093/gji/ggad068

Kanamori, H., Ross, Z. E., & Rivera, L. (2020). Estimation of radiated energy using the KiK-net downhole records - Old method for modern data. *Geophysical Journal International*, *221*(2), 1029–1042. https://doi.org/10.1093/gji/ggaa040

Katsumata, A. (2004). Revision of the JMA displacement magnitude. *Quarterly Journal of Seismology*, *67*, 1–10.

Katsumata, A. (1999). Attenuation Function of Displacement Amplitude for Magnitude Calculation. *Papers in Meteorology and Geophysics*, *50*(1), 1–14. https://doi.org/10.2467/mripapers.50.1

Katsumata, A, & Kamaya, N. (2003). Low-frequency continuous tremor around the Moho discontinuity away from volcanoes in the southwest Japan. *Geophysical Research Letters*, *30*(1), 20–21. https://doi.org/10.1029/2002GL015981

Kosuga, M., & Haruyama, T. (2018). Spectral characteristics of waveforms of deep low-frequency microearthquakes beneath northeastern Japan. *Prog. Abst. Seism. Soc. Japan*, S23-P22.

Kwiatek, G., Bulut, F., Bohnhoff, M., & Dresen, G. (2014). High-resolution analysis of seismicity induced at Berlín geothermal field, El Salvador. *Geothermics*, *52*, 98–111. https://doi.org/10.1016/j.geothermics.2013.09.008

Liu, Y., & Rice, J. R. (2005). Aseismic slip transients emerge spontaneously in three-dimensional rate and state modeling of subduction earthquake sequences. *Journal of Geophysical Research: Solid Earth*, *110*(B8), 1–14. https://doi.org/10.1029/2004JB003424

Madariaga, R. (1979). On the relation between seismic moment and stress drop in the presence of stress and strength heterogeneity. *Journal of Geophysical Research*, *84*(B5), 2243. https://doi.org/10.1029/JB084iB05p02243

Mueller, C. S. (1985). Source pulse enhancement by deconvolution of an empirical Green's function. *Geophysical Research Letters*, *12*(1), 33–36. https://doi.org/10.1029/GL012i001p00033

Munafò, I., Malagnini, L., & Chiaraluce, L. (2016). On the Relationship between M_{w} and M_{L} for Small Earthquakes. *Bulletin of the Seismological Society of America*, *106*(5), 2402–2408. https://doi.org/10.1785/0120160130

Nakajima, J., Hada, S., Hayami, E., Uchida, N., Hasegawa, A., Yoshioka, S., Matsuzawa, T., & Umino, N. (2013). Seismic attenuation beneath northeastern Japan: Constraints on mantle dynamics and arc magmatism. *Journal of Geophysical Research: Solid Earth*, *118*(11), 5838–5855. https://doi.org/10.1002/2013JB010388

Nakajima, J., & Hasegawa, A. (2021). Prevalence of Shallow Low-Frequency Earthquakes in the Continental Crust. *Journal of Geophysical Research: Solid Earth*, *126*(4). https://doi.org/10.1029/2020JB021391

Nakajima, J., Matsuzawa, T., Hasegawa, A., & Zhao, D. (2001). Three-dimensional structure of V p , V s , and V p / V s beneath northeastern Japan: Implications for arc magmatism and fluids. *Journal* *of Geophysical Research: Solid Earth*, *106*(B10), 21843–21857. https://doi.org/10.1029/2000JB000008

Nakamichi, H., Hamaguchi, H., Tanaka, S., Ueki, S., Nishimura, T., & Hasegawa, A. (2003). Source mechanisms of deep and intermediate-depth low-frequency earthquakes beneath Iwate volcano, northeastern Japan. *Geophysical Journal International*, *154*(3), 811–828. https://doi.org/10.1046/j.1365-246X.2003.01991.x

Obara, K. (2002). Nonvolcanic deep tremor associated with subduction in southwest Japan. *Science*, *296*(5573), 1679–1681. https://doi.org/10.1126/science.1070378

Okada, T., Umino, N., & Hasegawa, A. (2010). Deep structure of the ou mountain range strain concentration zone and the focal area of the 2008 Iwate-Miyagi Nairiku earthquake, NE Japan-seismogenesis related with magma and crustal fluid. *Earth, Planets and Space*, *62*(3), 347–352. https://doi.org/10.5047/eps.2009.11.005

Okada, T., Umino, N., & Hasegawa, A. (2012). Hypocenter distribution and heterogeneous seismic velocity structure in and around the focal area of the 2008 Iwate-Miyagi Nairiku Earthquake, NE Japan - Possible seismological evidence for a fluid driven compressional inversion earthquake. *Earth, Planets and Space*, *64*(9), 717–728. https://doi.org/10.5047/eps.2012.03.005

Prieto, G. A., Shearer, P. M., Vernon, F. L., & Kilb, D. (2004). Earthquake source scaling and self-similarity estimation from stacking *P* and *S* spectra. *Journal of Geophysical Research: Solid Earth*, *109*(B8). https://doi.org/10.1029/2004JB003084

Rivera, L., & Kanamori, H. (2005). Representations of the radiated energy in earthquakes. *Geophysical Journal International*, *162*(1), 148–155. https://doi.org/10.1111/J.1365-246X.2005.02648.X/2/M_162-1-148-IEQ053.JPEG

Rogers, G., & Dragert, H. (2003). Episodic tremor and slip on the Cascadia subduction zone: The chatter of silent slip. *Science*, *300*(5627), 1942–1943. https://doi.org/10.1126/SCIENCE.1084783/ASSET/DCC117CE-4CAD-4799-90C0-B9DFE257EA05/ASSETS/GRAPHIC/SE2431617002.JPEG

Ross, Z. E., Ben-Zion, Y., White, M. C., & Vernon, F. L. (2016). Analysis of earthquake body wave spectra for potency and magnitude values: implications for magnitude scaling relations. *Geophysical Journal International*, *207*(2), 1158–1164. https://doi.org/10.1093/gji/ggw327

Shearer, P. M., Abercrombie, R. E., & Trugman, D. T. (2022). Improved stress drop estimates for M 1.5 to 4 earthquakes in Southern California from 1996 to 2019. *Journal of Geophysical Research: Solid Earth*, 1–23. https://doi.org/10.1029/2022jb024243

Shearer, P. M., Prieto, G. A., & Hauksson, E. (2006). Comprehensive analysis of earthquake source spectra in southern California. *Journal of Geophysical Research: Solid Earth*, *111*(6), 1–21. https://doi.org/10.1029/2005JB003979

Shelly, D. R., Beroza, G. C., & Ide, S. (2007). Non-volcanic tremor and low-frequency earthquake swarms. *Nature*, *446*(7133), 305–307. https://doi.org/10.1038/nature05666

Shelly, D. R., Beroza, G. C., Ide, S., & Nakamula, S. (2006). Low-frequency earthquakes in Shikoku, Japan, and their relationship to episodic tremor and slip. *Nature*, *442*(7099), 188–191. https://doi.org/10.1038/nature04931

Snoke, J. A. (1987). STABLE DETERMINATION OF (BRUNE) STRESS DROPS. In *Bulletin of the Seismological Society of America* (Vol. 77, Issue 2). http://pubs.geoscienceworld.org/ssa/bssa/article-pdf/77/2/530/5333444/BSSA0770020530.pdf

Supino, M., Poiata, N., Festa, G., Vilotte, J. P., Satriano, C., & Obara, K. (2020). Self-similarity of low-frequency earthquakes. *Scientific Reports 2020 10:1*, *10*(1), 1–9. https://doi.org/10.1038/s41598-020-63584-6

Takahashi, T., Sato, H., Ohtake, M., & Obara, K. (2005). Scale dependence of apparent stress for earthquakes along the subducting pacific plate in northeastern Honshu, Japan. *Bulletin of the Seismological Society of America*, *95*(4), 1334–1345. https://doi.org/10.1785/0120040075

Thomas, A. M., Beroza, G. C., & Shelly, D. R. (2016). Constraints on the source parameters of low-frequency earthquakes on the San Andreas Fault. *Geophysical Research Letters*, *43*(4), 1464–1471. https://doi.org/10.1002/2015GL067173

Trugman, D. T. (2020). Stress-drop and source scaling of the 2019 ridgecrest, California, earthquake sequence. *Bulletin of the Seismological Society of America*, *110*(4), 1859–1871. https://doi.org/10.1785/0120200009

Trugman, D. T., & Shearer, P. M. (2017). Application of an improved spectral decomposition method to examine earthquake source scaling in Southern California. *Journal of Geophysical Research: Solid Earth*, *122*(4), 2890–2910. https://doi.org/10.1002/2017JB013971

Tsuchiyama, A., Taira, T., Nakajima, J., & Bürgmann, R. (2022). Emergence of Low-Frequency Aftershocks of the 2019 Ridgecrest Earthquake Sequence. *Bulletin of the Seismological Society of America*, 1–13. https://doi.org/10.1785/0120210206

Uchide, T., & Imanishi, K. (2018). Underestimation of Microearthquake Size by the Magnitude Scale of the Japan Meteorological Agency: Influence on Earthquake Statistics. *Journal of Geophysical Research: Solid Earth*, *123*(1), 606–620. https://doi.org/10.1002/2017JB014697

Ueno, H., Hatakeyama, S., Aketagawa, T., Funasaki, J., & Hamada, N. (2002). Improvement of hypocenter determination procedures in the Japan Meteorological Agency. *Quarterly Journal of Seismology*, *65*, 123–134.

Ukawa, M., & Ohtake, M. (1987). A monochromatic earthquake suggesting deep-seated magmatic activity beneath the Izu-Ooshima Volcano, Japan. *Journal of Geophysical Research*, *92*(B12), 12649. https://doi.org/10.1029/jb092ib12p12649

Vassilious.M.S., & Kanamori, H. (1982). The energy release in earthquakes. *Bulletin of the Seismological Society of America*, *72*(2), 371–387. https://doi.org/https://doi.org/10.1785/BSSA0720020371

Venkataraman, A., & Kanamori, H. (2004). Observational constraints on the fracture energy of subduction zone earthquakes. *Journal of Geophysical Research: Solid Earth*, *109*(B5), 5302. https://doi.org/10.1029/2003JB002549

Wech, A. G., Thelen, W. A., & Thomas, A. M. (2020). Deep long-period earthquakes generated by second boiling beneath Mauna Kea volcano. *Science*, *368*(6492), 775–779. https://doi.org/10.1126/SCIENCE.ABA4798/SUPPL_FILE/ABA4798_WECH_SM.PDF

Wessel, P., & Smith, W. H. F. (1998). New, improved version of generic mapping tools released. *Eos, Transactions American Geophysical Union*, *79*(47), 579–579.

Yoshida, K., Hasegawa, A., Noguchi, S., & Kasahara, K. (2020). Low-frequency earthquakes observed in close vicinity of repeating earthquakes in the brittle upper crust of Hakodate, Hokkaido, northern Japan. *Geophysical Journal International*, *223*(3), 1724–1740. https://doi.org/10.1093/gji/ggaa418

Yoshida, K., Hasegawa, A., Okada, T., & Iinuma, T. (2014)a. Changes in the stress field after the 2008 M 7.2 Iwate-Miyagi Nairiku earthquake in northeastern Japan. *Journal of Geophysical Research: Solid Earth*, *119*(12), 9016–9030. https://doi.org/10.1002/2014JB011291

Yoshida, K., Hasegawa, A., Okada, T., Takahashi, H., Kosuga, M., Iwasaki, T., Yamanaka, Y., Katao, H., Iio, Y., Kubo, A., Matsushima, T., Miyamachi, H., & Asano, Y. (2014)b. Pore pressure distribution in the focal region of the 2008 M7.2 Iwate-Miyagi Nairiku earthquake. *Earth, Planets and Space*, *66*(1), 1–7. https://doi.org/10.1186/1880-5981-66-59

Yoshida, K., & Kanamori, H. (2023). Time-domain source parameter estimation of *M*w 3–7 earthquakes in Japan from a large database of moment-rate functions. *Geophysical Journal International*, *234*(1), 243–262. https://doi.org/10.1093/gji/ggad068

Yoshida, K., Saito, T., Urata, Y., Asano, Y., & Hasegawa, A. (2017). Temporal Changes in Stress Drop, Frictional Strength, and Earthquake Size Distribution in the 2011 Yamagata-Fukushima, NE Japan, Earthquake Swarm, Caused by Fluid Migration. *Journal of Geophysical Research: Solid Earth*, *122*(12), 10,379-10,397. https://doi.org/10.1002/2017JB014334

Zhao, D., Horiuchi, S., & Hasegawa, A. (1990). 3-D seismic velocity structure of the crust and the uppermost mantle in the northeastern Japan Arc. *Tectonophysics*, *181*(1–4), 135–149. https://doi.org/10.1016/0040-1951(90)90013-X

Appendix-A

The procedure for the spectral ratio method

1. Select EGFs. We selected small events with magnitude differences greater than 1 which occurred within 3 km from the reference events as EGFs. Prior to this, we removed the reference events which have less than 10 EGFs and did not compute source corner frequency.

2. Calculate spectral ratio. We calculated the spectral ratio of the reference-EGF pairs for each station and component, and obtained representative spectral ratios using their geometric mean.

3. Estimate source corner frequency. We estimated source corner frequency of the reference events and EGFs by fitting model source spectra assuming the ω^2 model to the derived spectral ratio. Source corner frequencies were estimated at 0.1 Hz intervals from 0.5 Hz to 20 Hz using a grid search method.

Appendix-B

The relationship between estimated source corner frequency (f_c) and high-frequency falloff rate n

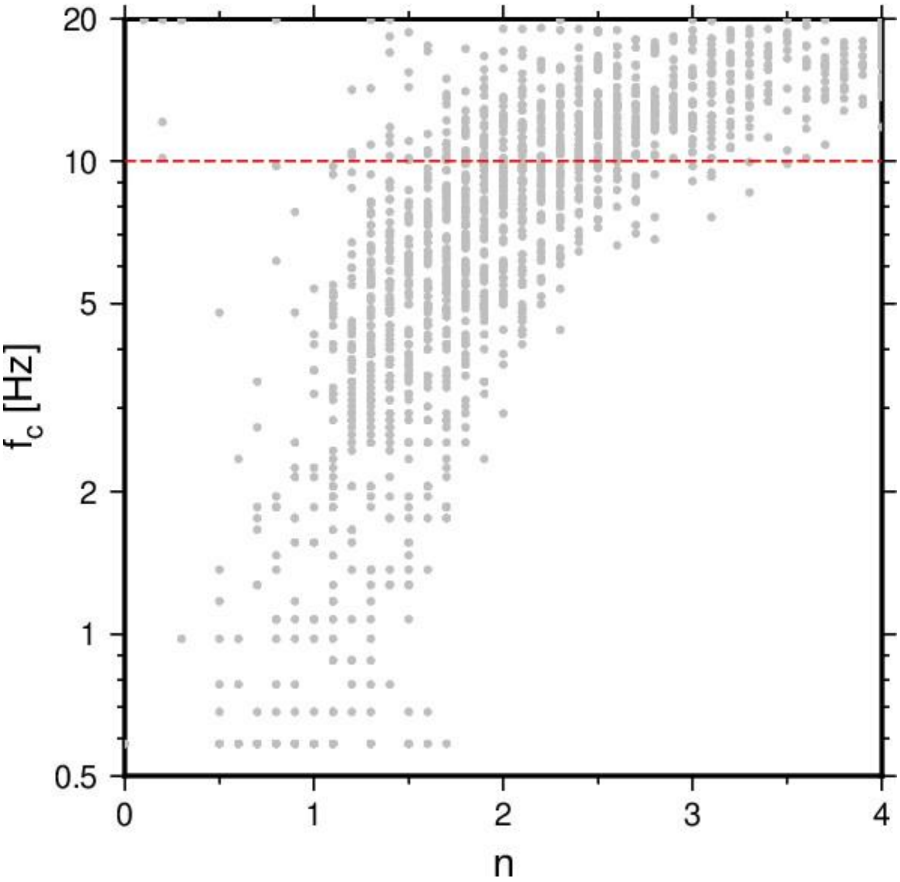

Figure B-1 The relationship between the estimated source corner frequency (f_c) and spectral high-frequency falloff rate (n) for regular earthquakes.